CrossMark

Radio, Hard X-Ray, and Gamma-Ray Emissions Associated with a Far-Side Solar Event

V.V. Grechnev[1] · **V.I. Kiselev[1]** · **L.K. Kashapova[1,2]** · **A.A. Kochanov[1,2]** ·
I.V. Zimovets[3,4,5] · **A.M. Uralov[1]** · **B.A. Nizamov[6,7]** · **I.Y. Grigorieva[8]** · **D.V. Golovin[3]** ·
M.L. Litvak[3] · **I.G. Mitrofanov[3]** · **A.B. Sanin[3]**

Abstract The far-side solar eruptive event SOL2014-09-01 produced hard electromagnetic and radio emissions that were observed with detectors at near-Earth vantage points. Especially challenging was a long-duration > 100 MeV γ-ray burst that was probably produced by accelerated protons exceeding 300 MeV. This observation raised the question how high-energy protons could reach the Earth-facing solar surface. Some preceding studies discussed a scenario in which protons accelerated by a shock driven by a coronal mass ejection high in the corona return to the solar surface. We continue with the analysis of this challenging event, involving radio images from the *Nançay Radioheliograph* and hard X-ray data from the *High Energy Neutron Detector* (HEND) of the *Gamma-Ray Spectrometer* onboard

---

✉ V.V. Grechnev
grechnev@iszf.irk.ru

I.V. Zimovets
ivanzim@iki.rssi.ru

I.Y. Grigorieva
irina.2014.irina@mail.ru

[1] Institute of Solar-Terrestrial Physics SB RAS, Lermontov St. 126A, Irkutsk 664033, Russia

[2] Irkutsk State University, Gagarin Blvd. 20, Irkutsk 664003, Russia

[3] Space Research Institute RAS, Profsoyuznaya St. 84/32, Moscow 117997, Russia

[4] State Key Laboratory of Space Weather, National Space Science Center (NSSC) of the Chinese Academy of Sciences, No. 1 Nanertiao, Zhongguancun, Haidian District, Beijing, 100190, China

[5] International Space Science Institute – Beijing (ISSI-BJ), No. 1 Nanertiao, Zhongguancun, Haidian District, Beijing, 100190, China

[6] Faculty of Physics, Lomonosov Moscow State University, Moscow, 119992, Russia

[7] Sternberg Astronomical Institute, Lomonosov Moscow State University, Universitetskii Pr. 13, Moscow, 119992, Russia

[8] Main Astronomical (Pulkovo) Observatory RAS, Pulkovskoe Sh. 65, St. Petersburg 196140, Russia

---

Springer

the *Mars Odyssey* space observatory located near Mars. HEND recorded unocculted flare emission. The results indicate that the emissions observed from the Earth's direction were generated by flare-accelerated electrons and protons trapped in static long coronal loops. They can be reaccelerated in these loops by a shock wave that was excited by the eruption, being initially not driven by a coronal mass ejection. The results highlight ways to address the remaining questions.

Keywords Flares, energetic particles · Magnetic fields, corona · Radio bursts · Waves, shock · X-ray bursts

1. Introduction

The source of solar energetic particles (SEPs) that are produced in solar eruptive-flare events is a subject of long-standing debate. SEPs consist of different species dominated by protons. Two sources of accelerated protons have been considered (see, *e.g.*, Kahler, 2001; Kallenrode, 2003; Aschwanden, 2012; Reames, 2013). One presumable origin of accelerated protons is associated with flare processes in solar active regions that manifest in X-rays and microwaves. Another source is related to a bow shock driven by the outer surface of a super-Alfvénic coronal mass ejection (CME). Many indications have been considered to identify the elusive source of accelerated protons. One of them is γ-ray emission, which was mostly observed concurrently with other flare emissions and seemingly favored the acceleration of protons in flares along with electrons (*e.g.* Ramaty and Mandzhavidze, 2000; Livshits and Belov, 2004; Chupp and Ryan, 2009; Kurt *et al.*, 2010; Vilmer, MacKinnon, and Hurford, 2011).

Flare emissions are observed in a wide electromagnetic range, from radio waves up to high-energy γ-rays. Gyrosynchrotron emission observed in the radio range and a broadband hard X-ray (HXR) and γ-ray bremsstrahlung continuum are produced by accelerated electrons. Accelerated protons and heavier ions can be recognized from discrete γ-ray lines. Of special interest is the π^0-decay emission. Neutral pions appear in proton–proton collisions, when the proton energy exceeds 300 MeV, and they rapidly decay into two photons, producing a Doppler-broadened wide enhancement in the γ-ray spectrum around 100 MeV in addition to the bremsstrahlung continuum (*e.g.* Ramaty, Kozlovsky, and Lingenfelter, 1975; Hudson and Ryan, 1995; Vilmer, MacKinnon, and Hurford, 2011). Thus, the π^0-decay emission is a direct indication of protons that are accelerated to high energies. Observations and identification of this γ-ray emission are only possible with high sensitivity and sufficient spectral measurements at high energies. For this reason, fewer than 20 events have been confidently identified with π^0-decay emission in the past (*e.g.* Ryan, 2000; Grechnev *et al.*, 2008b; Chupp and Ryan, 2009; Kurt *et al.*, 2010; Kuznetsov *et al.*, 2011).

Being temporally close to flare emissions produced by accelerated electrons, discrete nuclear γ-ray lines, and especially the π^0-decay emission, have been considered as evidence of proton acceleration in flares. On the other hand, γ-ray emission much longer than the HXR burst was observed in a few events (*e.g.* Forrest *et al.*, 1985; Akimov *et al.*, 1996; Ryan, 2000). A challenge to the flare-related origin of γ-ray emission was provided by the observation of γ-ray emission from an event behind the solar limb. To explain this phenomenon, Cliver, Kahler, and Vestrand (1993) proposed that protons accelerated by a CME-driven shock wave on an open magnetic field partly escaped into interplanetary space and partly returned to the solar surface, precipitating far from the flare region.

With the advent of the *Fermi Gamma-Ray Space Telescope* mission in 2008, high-sensitivity γ-ray observations became available with comprehensive spectral information and coordinate measurements of γ-ray photons at > 100 MeV by the *Large Area Telescope* (LAT: Atwood *et al.*, 2009). Although it is a non-solar mission, *Fermi* also provides rich information for solar studies. *Fermi* has shown that γ-ray emissions are quite common in solar flares. Thirty long-duration γ-ray events have been observed (Share *et al.*, 2017). Pesce-Rollins *et al.* (2015) reported on the detection by *Fermi*/LAT of high-energy γ-ray emissions from three behind-the-limb solar flares on 11 October 2013, 6 January 2014, and 1 September 2014. These events were addressed by Ackermann *et al.* (2017). The π^0-decay emission was identified with confidence in two of them: SOL2013-10-11 and SOL2014-09-01. The authors invoked the idea of Cliver, Kahler, and Vestrand (1993) to interpret these emissions.

Plotnikov, Rouillard, and Share (2017) elaborated on this idea in their analysis of the three events. Among the issues that they analyzed by means of three-dimensional reconstructions of coronal shock fronts, the authors showed the events' magnetic connectivity to the Earth-facing solar surface. Ackermann *et al.* (2017) and Plotnikov, Rouillard, and Share (2017) considered coronal shocks to be driven by fast CMEs and emphasized that the CME and associated shock wave were fastest in the 1 September 2014 event, where the high-energy γ-ray emission was strongest.

On the other hand, Hudson (2018) pointed out basic problems of the scenario proposed by Cliver, Kahler, and Vestrand (1993). First, a high mirror ratio at the base of an open coronal structure prevents the back-precipitation of particles from large coronal heights, so that only a small part of the protons is able to return to the Sun in this scheme. Second, the total number of high-energy protons estimated for a set of SEP events appears to be insufficient to sustain the high-energy γ-rays in the events addressed by Ackermann *et al.* (2017).

To explain the long-duration γ-rays from occulted events, Hudson (2018) considered two options. In the "lasso" scenario, some SEPs are captured in a noose that extends to several solar radii and then retracts. In this scenario, trapped particles acquire energy due to the betatron acceleration and first-order Fermi process. The second option that he proposed is a "coronal thick target" scenario, in which protons trapped in a static volume generate pions and γ-ray continuum. As Hudson (2018) estimated, this can proceed for a few hours.

Analyzing the dynamic evolution of the global magnetic field and the shock wave considered to be CME-driven, Jin *et al.* (2018) simulated the CME in the 1 September 2014 event using a global magnetohydrodynamics (MHD) model. The authors concluded that particles responsible for the high-energy γ-ray emission were accelerated in the CME environment and escaped the shock downstream region along magnetic fields that were connected to the solar surface far away from the flaring region.

We therefore conclude that in spite of the rich observational data currently available and the great efforts that have been applied, the source of accelerated protons escapes identification. Furthermore, examining the alternative of a flare *versus* CME-driven shock, the researchers base their considerations on a simplified traditional scheme in which the bow shock is excited by the outer surface of a fast CME. However, recent studies show that coronal shock waves are initially excited by sharply erupting flux-ropes inside the developing CMEs, while reconnection processes underneath produce a flare (see, *e.g.*, Grechnev *et al.*, 2016, 2018 for details and review). The flare, CME, and shock-formation processes are expected to be tightly associated, which determines the close relation between the characteristics of flares, CMEs, and shock waves. The situation becomes still more complicated.

If flare processes are responsible for proton acceleration, then CME parameters are misleading. If shock acceleration is at work, then the acceleration starts earlier and at lower

altitudes than assumed previously. If both sources are implicated, then untangling their contributions is still more difficult.

Keeping in mind these circumstances, we continue with the analysis of the 1 September 2014 event. It was observed from different vantage points. From the Earth's direction, the HXR burst was observed by the *Fermi Gamma-ray Burst Monitor* (GBM: Meegan *et al.*, 2009) and the *Wind/Konus Gamma-Ray Burst Experiment* (Aptekar *et al.*, 1995). A radio burst dominated by the gyrosynchrotron (GS) emission at frequencies > 300 MHz was recorded by the *Radio Solar Telescope Network* (RSTN: Guidice, 1979; Guidice *et al.*, 1981), while its source was observed at the *Nançay Radioheliograph* (NRH: Kerdraon and Delouis, 1997). The GS burst was considered by Ackermann *et al.* (2017) and Carley *et al.* (2017). The unoccluded flare emission was recorded from the Martian direction by the *High Energy Neutron Detector* (HEND) of the *Gamma-Ray Spectrometer* onboard the *Mars Odyssey* space observatory (Boynton *et al.*, 2004). The SOL2014-09-01 event was not listed in the HEND catalog (Livshits *et al.*, 2017); nevertheless, HEND did observe it.

Based on these data, we analyze the electromagnetic emissions observed, endeavor to determine their possible sources, try to understand the causes of the long-lasting emissions, and reveal the history and possible role of the shock wave. In this way, we pursue understanding which of the scenarios that have been proposed match the observations. We specify and refine some of the results and conclusions drawn previously.

Section 2 addresses electromagnetic emissions observed in the event and their probable sources. Section 3 analyzes shock waves and their kinematics. Section 4 discusses the results and their interpretation. Section 5 summarizes the findings and presents the conclusion.

2. Electromagnetic Emissions and Their Sources

2.1. Overview of the Event

The eruptive flare occurred in an active region (AR) located behind the east limb at a position of N14 E126 estimated by Ackermann *et al.* (2017) or N14 E129 according to our estimate. The AR was numbered 12158 when it became visible from Earth. The flare was visible from different vantage points. It was observed from the STEREO-B spacecraft of the twin *Solar Terrestrial Relations Observatory* (STEREO: Kaiser *et al.*, 2008). STEREO-B was located 161° eastward of Earth. The vantage point of HEND onboard the *Mars Odyssey* was located 65.3° eastward of Earth.

Figure 1a presents the flare (bright streak) as observed in 195 Å by the *Extreme Ultraviolet Imager* (EUVI: Howard *et al.*, 2008) onboard STEREO-B. As the figure shows, the flare emission was not occulted for STEREO-B and HEND. According to Plotnikov, Rouillard, and Share (2017), the flare started in soft X-rays at about 10:54 and peaked at about 11:11 (all times are henceforth adjusted to observations from 1 AU and referred to UTC). The GOES importance of the flare estimated indirectly from STEREO-B/EUVI 195 Å data ranged from X1.0 (Chertok, Belov, and Grechnev, 2015) to X2.4 estimated by Ackermann *et al.* (2017) using the method of Nitta *et al.* (2013).

Figure 1b exemplifies the observations by the *Atmospheric Imaging Assembly* (AIA: Lemen *et al.*, 2012) onboard the *Solar Dynamics Observatory* (SDO) located at a near-Earth vantage point. For the analysis we mostly used the quarter-resolution level 1.5 synoptic AIA data available at jsoc.stanford.edu/data/aia/synoptic/ in steps of two minutes. The AIA 211 Å image ratio in Figure 1b presents the early liftoff of the CME. The projected position of the far-side active region is denoted by the cross. The dot denotes the *Fermi*/LAT > 100 MeV
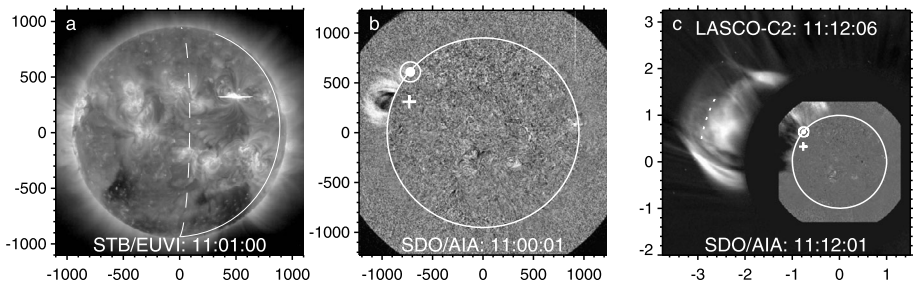
Figure 1 SOL2014-09-01 event observed from different vantage points. (**a**) The flare observed by STERE-O-B/EUVI in 195 Å. The meridian outlined with the *solid arc* is at a heliolongitude of $-90°$, approximately corresponding to the east limb visible from Earth. The *dashed arc* at $-155.3°$ corresponds to the east limb visible from Mars. (**b**) The early CME liftoff in an SDO/AIA 211 Å image ratio. The *cross* denotes the projected position of the flare site. (**c**) CME in a LASCO-C2 image with an inserted cotemporal AIA 211 Å image ratio. The *dotted arc* outlines the CME core at position angles $73° \pm 10°$ according to the measurements presented in Figure 2f. The *dot* in panels **b** and **c** denotes the *Fermi*/LAT > 100 MeV emission centroid position with the 68% error circle (from Ackermann *et al.*, 2017). The *axes* indicate the distance from solar disk center in arcseconds in panels **a** and **b** and in solar radii in panel **c**.

emission centroid position with the 68% error circle measured by Ackermann *et al.* (2017). The error circle characterizes the measurement accuracy and should not be confused with the scatter in the positions of individual γ-ray photons, which occupy a very large area of several solar disks. The *Fermi*/LAT centroid position is commented on in Section 4.2.

Figure 1c shows the CME observed by the *Large Angle Spectroscopic Coronagraph* (LASCO: Brueckner *et al.*, 1995) onboard the *Solar and Heliospheric Observatory* (SOHO) with an inserted cotemporal 211 Å image ratio. The dotted arc outlines the CME core at position angles $73° \pm 10°$ according to the measurements presented in Figure 2f. The average speed of the fastest CME feature measured in the online CME catalog (cdaw.gsfc.nasa.gov/CME_list/: Yashiro *et al.*, 2004) at position angles from 76° to 60° was about 1900 km s^{-1} with a strong average deceleration of -240 m s^{-2}. These properties indicate that the measurements in the CME catalog are related to a shock wave (Grechnev *et al.*, 2011b).

It is difficult to detect any erupting feature in EUVI 195 Å images, whereas infrequent imaging in different EUVI channels missed the event. Nevertheless, the AIA 131 Å images in Figures 2a–2e reveal a blob rising radially from behind the limb. The dashed lines bound the angular extend of the blob $73° \pm 5°$ with a central position angle denoted by the straight black line. After an apparent fast initial three-dimensional expansion, the blob did not laterally exceed the dashed lines by 11:02:00.

The blob is only visible in 131 Å and not detectable in any other channels. The temperature sensitivity characteristics of the AIA channels (Lemen *et al.*, 2012) thus suggest a blob temperature of about 10 MK. Most likely, this was an erupting flux rope. Hot flux ropes have previously been observed in 131 Å (*e.g.* Cheng *et al.*, 2011; Zimovets *et al.*, 2012; Patsourakos, Vourlidas, and Stenborg, 2013; Grechnev *et al.*, 2016). The structure of the blob is indiscernible; nevertheless, the AIA observations allow us to infer its kinematics.

Figures 2f–2h present probable kinematical plots of the blob inferred from the AIA 131 Å observations within the shaded interval by fitting an analytic function to the observed motion. We used a Gaussian acceleration pulse, while its actual shape is uncertain because of the double integration in the transition from the acceleration to the distance–time de-
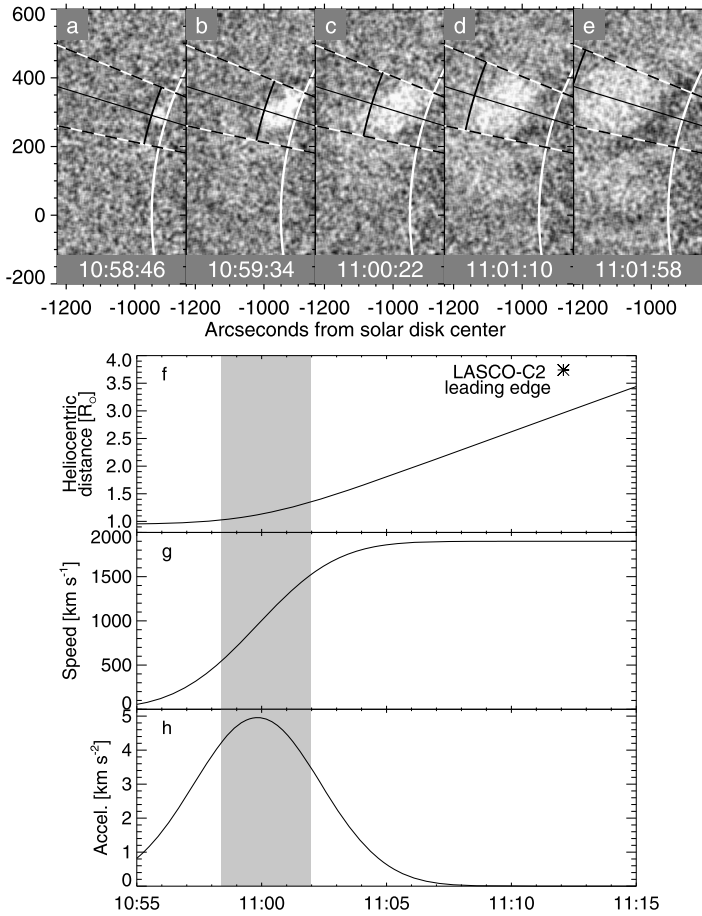
Figure 2 (**a**–**e**) Rising blob in AIA 131 Å image ratios (each divided by a fixed pre-event image observed at 10:58:22). The *white circles* denote the solar limb. The *black arcs* outline the leading edge of the blob. The *dashed lines* bound the angular extent of the blob $73° ± 5°$ with a central position angle denoted by the *straight black line*. (**f**–**h**) Probable kinematical plots of the blob. The *asterisk* in panel **f** represents the first CME measurement in the CME catalog. The shading represents the interval where the blob was measured within the AIA field of view.

pendence. The technique with which we inferred the kinematics is similar to that used by Grechnev *et al.* (2015, 2016, 2018).

The initial velocity of the blob was close to zero. Its final velocity is determined by the position of the CME core in the first LASCO-C2 image, where it appeared; the CME frontal structure behind the wave trace corresponds to the pre-eruption arcade enveloping the flux-rope progenitor. The difference between the final and initial velocities is equal to the integral over the acceleration pulse. Its duration (and maximum) is adjusted in attempts to reproduce, on average, the accelerating motion of the blob, which is barely visible within the AIA field of view.

The fit is shown in Figures 2a – 2e by the black arcs. The blob underwent a maximum acceleration around 10:59:40 and reached a final speed of $1900 ± 150 \, \mathrm{km \, s^{-1}}$. The uncertainty in the duration and maximum of the Gaussian acceleration pulse is within a factor of two.

Figure 3 Electromagnetic emissions observed from different vantage points. (**a**) Unocculted flare HXR burst recorded from the Martian direction by HEND (*black*), microwave burst at 5 GHz recorded at San Vito (*red*), and > 100 MeV γ-ray burst recorded by *Fermi*/LAT (*thick blue*). (**b**) Comparison of the HXR (*Wind/Konus*, *black*) and microwave (San Vito 8.8 GHz, *red*) bursts observed from the Earth's direction (similar to Figure 5 in Ackermann *et al.*, 2017). (**c**) Higher-energy HXR burst recorded by *Fermi*/GBM (similar to Figure 3 in Plotnikov, Rouillard, and Share, 2017).
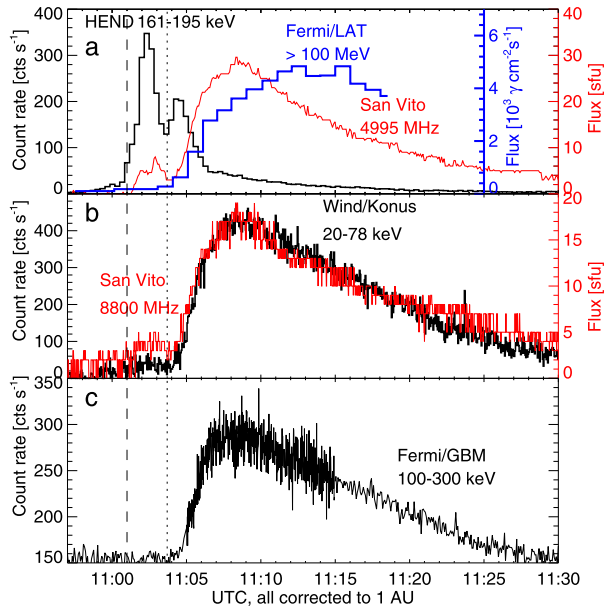

Figure 2 shows that when the acceleration ceased, the blob lagged behind the CME leading edge measured in the CME catalog by a factor of 1.45 at the first CME appearance in the LASCO-C2 field of view. The leading edge of the blob at that time according to the kinematics presented in Figures 2f – 2h is denoted in Figure 1c with a dotted arc, which corresponds to the CME core. We asserted the association of an erupting flux rope with the CME core previously, which does not contradict the traditional idea relating the flux rope to the cavity; the flux rope forms in the cavity from the structures of the core in the course of a time-extended process (Kuzmenko and Grechnev, 2017).

2.2. Temporal Profiles of the Bursts

Figure 3 presents the bursts observed in microwaves, HXR, and > 100 MeV γ-rays from different vantage points. Figure 3a shows the unocculted HXR burst recorded by HEND in a range of 50 – 800 keV with a temporal sampling of 20 seconds. The HXR burst comprised two overlapping impulsive peaks, each of about 1.5 minutes, followed by a long-lasting weaker gradual decay. The first peak occurred around 11:02:20 and the second around 11:04:30.

The microwave burst observed by RSTN from Earth exhibits the first minor peak corresponding to the first unocculted HXR peak around 11:02:20. The main microwave burst started nearly simultaneously with the second unocculted HXR peak around 11:04:30 but looks strongly stretched and lasted for about half an hour. This behavior suggests confinement of emitting electrons in a magnetic trap after an initial impulsive injection during the second unocculted HXR peak. The behavior of the high-energy γ-ray burst appears to be similar to the microwave burst; it started nearly simultaneously with the second HXR peak, and was still more strongly stretched.

The microwave burst and a lower-energy HXR burst observed from the Earth's direction by *Wind/Konus* (Figure 3b) were almost identical in shape, with the first minor peak and main long-duration burst. The main HXR burst observed by *Fermi*/GBM at higher energies was similar, while the first minor peak was indistinct.

Figure 4 Evolution of the
microwave emission during the
event. (**a**) Total-flux temporal
profile recorded at San Vito at
2.7 GHz. (**b**) Variations of the
microwave peak frequency.
(**c**) Power-law index of
microwave-emitting electrons
estimated from the slope of the
GS spectrum (ultrarelativistic
limit *solid*, semirelativistic case
dashed). The error ranges are
shown with *gray shadings*.
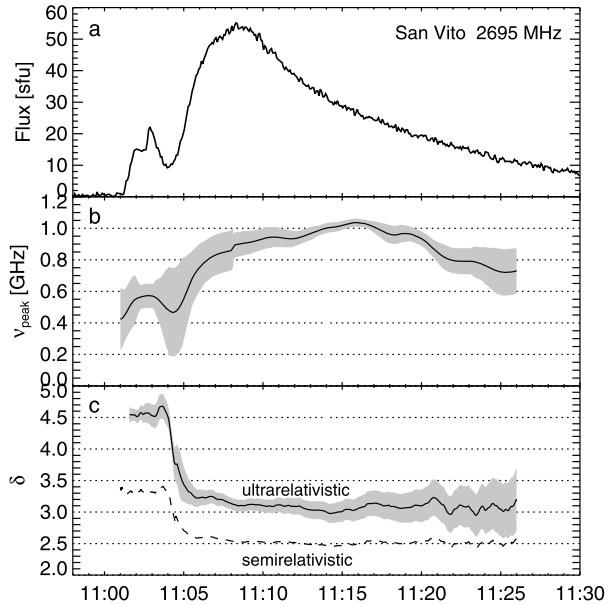
The photon spectrum index [γ] estimated from the HEND data was 3.27 for the first
peak and 3.13 for the second peak, and then it gradually hardened down to ≈ 2.2 at 11:15,
resembling the soft–hard–harder spectral behavior (Kiplinger, 1995). The photon-index er-
ror caused by the dead-time correction uncertainty does not exceed 0.3. Thus, the spectrum
indices of the two unoccultuded HXR peaks were almost identical. On the other hand, the main
long-duration burst visible from the Earth's direction was obviously harder in HXR than the
main burst. According to Ackermann *et al.* (2017), the emission spectrum integrated be-
tween 11:02 and 11:20 corresponded to a single power-law from 30 keV to about 10 MeV
with an index of 2.06. This value is close to the index estimated from HEND data for a later
stage of the event.

Figure 4 presents microwave spectral characteristics in comparison with the temporal
profile at 2695 MHz. The variations in the peak frequency [ν_{peak}] of the GS emission shown
in Figure 4b were computed by fitting in the log–log scale of a parabola to an instanta-
neous set of samples recorded at different frequencies at San Vito (see, *e.g.*, White *et al.*,
2003; Grechnev *et al.*, 2013a). The shading represents the measurement errors caused by
the background-level uncertainties and noise, and it does not include the calibration un-
certainties, which are not known. The peak frequency in the first minor peak was about
500 MHz. During the main burst, ν_{peak} increased but did not show large variations, being
within 700 – 1000 MHz.

Figure 4c presents the power-law index of the electron energy density (electron number)
spectrum estimated from the microwave index [α] at optically thin frequencies considerably
exceeding ν_{peak}. Usually such estimates invoke the semirelativistic approximation by Dulk
and Marsh (1982) (gyrosynchrotron emission), $\delta = 1.36 - 1.1\alpha$, where α is signed and δ is
always positive. The dashed line in Figure 4c represents δ estimated in this way. On the other
hand, according to Ackermann *et al.* (2017) and Plotnikov, Rouillard, and Share (2017), a
single power-law electron spectrum exceeded 10 MeV during the main burst and extended
up to about 7 MeV during the first minor peak (Carley *et al.*, 2017). Thus, the ultrarelativistic
limit (synchrotron emission) estimate might be more applicable. In this case, $\delta = 1 - 2\alpha$

(Dulk, 1985). Figure 4c shows this estimate by the solid line with uncertainties represented by the gray shading. While the synchrotron emission matches the situation better, we use the term gyrosynchrotron following tradition.

For the thick-target emission in the non-relativistic limit corresponding to the HEND observations, the electron-number index $\delta = \gamma + 1.5 \approx 4.7$ (+0.5 relative to the electron-flux spectrum; see Silva, Wang, and Gary, 2000; White *et al.*, 2011). This value is close to the power-law index of microwave-emitting electrons in the first minor peak (the GS emission is mainly produced by the high-energy part of the electron spectrum). However, a much harder electron spectrum is suggested by the main burst. Progressive hardening of the electron spectrum down to $\delta - 3/2$ is possible in a magnetic trap, where particles are injected continuously (Melrose and Brown, 1976; Melnikov and Magun, 1998; Metcalf and Alexander, 1999). However, if we indeed consider trapping here, then the main injection was impulsive, while the variations in δ inferred from the microwave spectrum after 11:05 seem to be too small to account for the difference between the electron spectra in the flare HXR peak and main radio burst.

This source of the main burst was apparently different from the source of the first minor peak. With an almost constant electron-spectrum index and nearly constant peak frequency during the main burst, its source must be static. The gradual changes in the peak frequency could be due to a varying number of emitting electrons and minor variations in the electron spectrum. This behavior does not support a possible association of the emitting source with either the CME, whose flux-rope moved away from the solar surface up to $\approx 3\,\mathrm{R}_\odot$ at 11:24, when the burst still continued, or a CME-related shock wave.

To summarize, the flare was comprised of two main acceleration episodes manifested in the HXR peaks observed by HEND. The first episode accounts for the first minor peak of the emissions observed from the Earth's direction. The second flare episode coincides with the onset of the main burst in all emissions observed from near-Earth vantage points. This burst was much longer than the flare HXR peak, which suggests a possible confinement of emitting particles in a magnetic trap injected there during the second flare episode. The > 100 MeV γ-ray burst shows a similar behavior to the HXR and GS burst, suggesting a common location of emitting electrons and protons. Plotnikov, Rouillard, and Share (2017) also concluded that accelerated electrons and protons had a common source. The spectrum of these particles was considerably harder than during the second flare peak. If the second flare-acceleration episode supplied particles responsible for the main burst, then additional acceleration was required.

2.3. Radio Sources

Ackermann *et al.* (2017) showed that the radio burst was dominated by the gyrosynchrotron emission even in the metric range, at frequencies $> 200 - 300$ MHz. This enabled the use of observations from the *Nançay Radioheliograph* (NRH) in the analysis of the GS source presented by Carley *et al.* (2017). The authors revealed an off-limb GS source with a large extent centered above the flare position. The source appeared by 11:01 and remained centered at this position until about 11:05, expanding along the limb to occupy the position angles from approximately $50°$ to $87°$ at 11:02. This time interval corresponds to the first minor peak. After 11:05, the authors found a motion of the centroid position of the source southward with a speed of ≈ 1500 km s^{-1}, while its height was almost unchanged. The authors related this GS source to the CME.

The hot blob in Figure 2 apparently corresponded to the CME flux rope, being the most probable candidate for a CME-related GS source. However, the blob rose radially and did
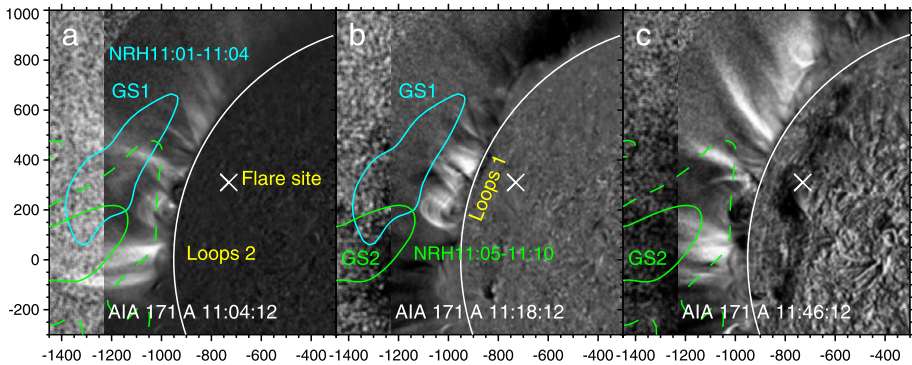
Figure 5 Coronal loops in AIA 171 Å and SWAP 174 Å images. Gyrosynchrotron sources observed by NRH at 432 MHz are shown by the color contours. The *blue contours* represent the first source (GS1) at a level of 0.6 of its maximum brightness. The *green contours* represent the second source (GS2) at levels of 0.6 (*solid*) and 0.22 (*dashed*; panels **a** and **c**) of its maximum brightness. The *slanted cross* denotes the projected position of the flare site.

not laterally exceed a narrower range of position angles from 68° to 78° by 11:02. This behavior is incompatible with that of the radio source reported by Carley *et al.* (2017).

To understand the situation, we produced the images from ten-second integrated NRH data using the SolarSoft NRH package (secchirh.obspm.fr/nrhpackage.php) at 327 MHz and 432 MHz during 11:00 – 11:10 with an integration time and steps of 30 seconds. The images at both frequencies show that one nearly static source (GS1) appeared at about 11:01 and faded until about 11:05, when another static source (GS2) appeared. This source was located approximately above the Equator and had a smaller extent along the limb. GS2 was detectable until at least 11:10.

We did not consider a lateral expansion of GS1 that Carley *et al.* (2017) detected in their higher-resolution images. This expanding component resembles in behavior the EUV wave propagation (see the Electronic Supplementary Material AIA211_EUV_waves.mpg) and might be due to a possible Type II precursor continuum or another emission not related to relativistic electrons. Thus, the fast southward motion of the centroid position found by Carley *et al.* (2017) was most likely caused by a change in the brightness distribution among the two nearly static sources.

Neither GS1 nor GS2 exhibited any significant displacement, while their possible minor motions are beyond our scope. Figure 5 presents the contours of the NRH images averaged over the first minor peak duration for GS1 and over an interval of 11:05 – 11:10 for GS2, corresponding to a considerable part of the main burst, including its maximum. Each of the two sources considerably exceeded the NRH beam size; thus, the NRH images represent their realistic dimensions.

To reveal the coronal structures with which each of the two sources was associated, we invoke the coronal-dimming phenomenon. The CME liftoff rapidly stretches closed structures, leaving density depletion behind it. This process shows up as dimming, whose development is visible in the left panel of the AIA211_EUV_waves.mpg Electronic Supplementary Material. This panel in the movie presents the ratios of each current image to a fixed image observed before the event. A large dimmed area expanded in the movie. The dimming depth increased by about 11:10, and then the coronal-plasma density started to recover. Dividing AIA images by the deepest-dimming image at 11:10 emphasizes the coronal structures that initially faded and then reappeared.

The AIA 171 Å image ratios in Figure 5 are shown for three times corresponding to the deepening of the dimming in Figure 5a and its recovery in Figures 5b and 5c. The field of view is extended to the left using 174 Å images produced by the *Sun Watcher using Active Pixel System detector and Image Processing* (SWAP: Berghmans *et al.*, 2006) onboard the *Proba 2* micro-satellite.

Source GS1 was associated with the uppermost part of a far-side arcade denoted Loops 1, whose top is visible above the limb. The near-the-limb portion of GS1 is most likely invisible because of refraction. Source GS2 was associated with different long loops denoted Loops 2, which are deflected by the rising CME in Figure 5a and relaxed to an equilibrium state in a much later Figure 5c. We did not analyze a possible small deviation in the position of GS2 that would correspond to the minor motions of the loops. No on-disk manifestations are visible in the NRH images, except for a lower-frequency ($\lesssim 300$ MHz) static noise-storm source in the southern part of the Sun that was irrelevant to the eruptive event in question (Carley *et al.*, 2017).

Thus, a static source GS1 was responsible for the first minor peak around 11:02:20. Carley *et al.* (2017) found that this peak was caused by the GS emission from electrons with a power-law index $\delta = 3.2$ in an energy range from 9 keV to 6.6 MeV in a magnetic field of 4.4 G and an ambient plasma density of $n_0 = 1.3 \times 10^8$ cm^{-3}. This power-law electron spectrum index is close to the semirelativistic approximation in our Figure 4c, while the peak frequency in Figure 4b estimated from the San Vito data is somewhat lower than Carley *et al.* (2017) found from the Sagamore Hill fluxes reduced because of operational issues. The peak frequency here is strongly affected by the Razin suppression, which is determined by the ambient plasma density. It was depleted at this time because of the developing dimming; thus, the parameters estimated by Carley *et al.* (2017) are most likely correct with a reduced ambient plasma density.

Another off-limb static source, GS2, was responsible for the main long-duration burst. To estimate its parameters, we used the GX simulator of the GS emission (Kuznetsov, Nita, and Fleishman, 2011). The best fit of the actual radio spectrum near the maximum at 11:08 is reached with a magnetic-field strength of about 1 G, electrons with an index of $\delta \approx 2.8$, which lies between the two approximations in Figure 4c, a low-energy cutoff on the order of 100 keV, and an ambient density of a few 10^8 cm^{-3}. The simulations indicate that both bases of the emitting loops were most likely occulted; with an on-disk position for at least one of them, the fluxes around the peak frequency become flatter than the observations show.

There were no on-disk signatures of the GS emission. If it had been produced by returning electrons accelerated by a shock wave that expanded away from the Sun (the scenario advocated by Plotnikov, Rouillard, and Share, 2017 and Jin *et al.*, 2018), then the source should move across the solar surface, as Hudson (2018) pointed out. This situation is not observed.

In summary, the GS sources observed by NRH confirm the indications provided by the temporal profiles. Sources GS1 and GS2 were distinct, each of them was nearly static and located off-limb, and none of them was associated with the structures of the rising CME. Source GS1 emitted by closed loops was related to the first HXR flare peak and did not show any significant trapping. The long-lived source GS2 appeared in a different, higher, closed structure during the second HXR flare peak, which probably initiated the main burst visible from the Earth's direction. The region of the GS2 radio source is also the most probable candidate for the long-duration HXR and > 100 MeV γ-ray emissions. In contrast to the first peak, the main burst is suggestive of a prolonged confinement of emitting particles in a magnetic trap.
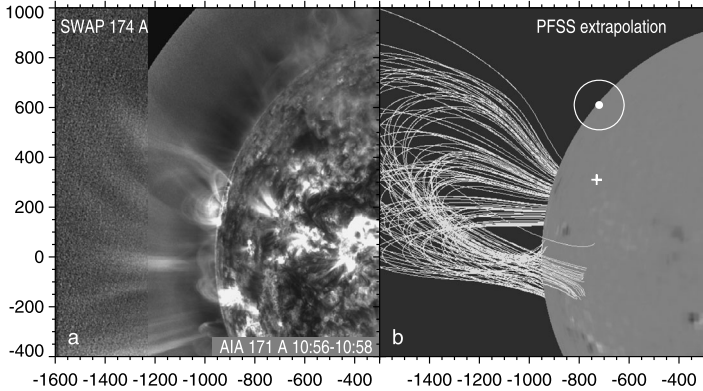
Figure 6 Coronal loops in a combined pre-event EUV image composed from AIA 171 Å and SWAP 174 Å images (**a**) and closed magnetic-field lines extrapolated from the flare site using the PFSS model (**b**). The *cross* denotes the projected position of the flare site. The *dot* denotes the *Fermi*/LAT > 100 MeV emission centroid position with the 68% error circle (from Ackermann *et al.*, 2017).

2.4. Coronal Configuration

To analyze the coronal configuration, we compare the coronal loops observed in the EUV with magnetic-field lines extrapolated from photospheric magnetograms produced by the *Helioseismic and Magnetic Imager* (HMI: Scherrer *et al.*, 2012) on SDO. We used the potential field source surface (PFSS) model from the SolarSoft package provided by the Lockheed Martin Solar and Astrophysics Laboratory (LMSAL: www.lmsal.com/~derosa/pfsspack/). Because the flare-hosting AR 12158 was located behind the east limb, extrapolation is only possible from a synoptic magnetogram. We used a magnetogram for Carrington Rotation 2155, in which AR 12158 was mapped about ten days after the event, being not yet present in the previous-rotation magnetogram. Analysis of open magnetic fields over a large part of the solar surface has led to results very similar to those presented by Plotnikov, Rouillard, and Share (2017).

For the comparison we produced a combined image of coronal loops observed in EUV before the event. It is shown in Figure 6a. The main part of the image is an average over two AIA 171 Å images divided by the azimuthally averaged radial brightness distribution (the technique is described by Kochanov *et al.*, 2013). The field of view is extended by an enhanced-contrast average over 11 SWAP 174 Å images observed from 10:31:21 to 10:55:12. Figure 6b presents a set of loops extrapolated from a small region embracing the flare site.

The long loops visible in EUV near the limb close to the Equator (Figure 6a, $y \approx 0''$) are acceptably well reproduced by the extrapolated-field lines in Figure 6b. The lowest loops of the presented set are comparable in length with the solar radius, and the others are even longer. All of these loops emanate from the flare site. For some of them, the opposite ends are rooted behind the limb, and some others come to the visible side near the Equator. Comparison with Figure 5 shows that the gyrosynchrotron source GS2, which is responsible for the main long-duration burst, was located in these long loops. Their Earth-facing legs, visible around $y \approx 0''$, produced a brighter radio emission.

The region of the *Fermi*/LAT > 100 MeV centroid position and its wide environment were entirely covered by closed field lines over a wide range of altitudes. None of the field lines were connected with the flare site. Neither were there any open magnetic fields. For

clarity, we do not show the field lines in this region. It was located within a very large magnetic domain that was isolated from the domain in which the flare region resided.

The potential-field extrapolation used here (as well as force-free methods) is not able to reproduce the magnetic configuration during the CME eruption, which is the strongest violation of stationary conditions. The violation typically involves a nearby environment of the eruption region. In rare cases, which we call anomalous eruptions, reconnection occurs between an erupting structure and the large-scale coronal environment (*e.g.* Grechnev *et al.*, 2008a, 2011a, 2013b, 2014b; Uralov *et al.*, 2014). Typical manifestations of an anomalous eruption are the dispersal of the erupted material over a considerable part of the solar surface and microwave depressions (so-called negative bursts). Such phenomena are best visible in the 304 Å channel; in exceptional cases, they are manifested in all EUV channels (*e.g.* the SOL2011-06-07 event: Grechnev *et al.*, 2013b; van Driel-Gesztelyi *et al.*, 2014). We examined all EUV channels of STEREO/EUVI and SDO/AIA on 1 September 2014, but failed to find any manifestations of dispersed or returning erupted material. Neither was there any microwave depression. Thus, we did not find clear support from EUV or microwave observations for the scenario proposed by Jin *et al.* (2018). Furthermore, presumable reconnection in this scenario between the erupting structure and the domain, where the *Fermi*/LAT > 100 MeV centroid was located, had to proceed very deep into the closed-field area to reach the connection to the photosphere.

3. Shock Waves

The presence of a shock wave in this event is indicated by the high speed measured for the leading edge of the CME in the online CME catalog (cdaw.gsfc.nasa.gov/CME_list/: Yashiro *et al.*, 2004). Plotnikov, Rouillard, and Share (2017) measured some of the shock-wave characteristics based on three-dimensional reconstructions of the wave front from EUV and coronagraph observations. A shock wave can also be manifested in a Type II burst and EUV wave. As shown previously (*e.g.* Grechnev *et al.*, 2008a, 2011b, 2016, 2017, 2018), these signatures can be reconciled kinematically with each other and with a halo embracing a fast CME. Here we consider the shock-wave traces observed in EUV and coronagraph images and possible shock signatures in a dynamic radio spectrum.

3.1. Shock-Wave Signatures in EUV and Coronagraph Images

Figure 7 and the Electronic Supplementary Material AIA211_EUV_waves.mpg present EUV wave propagation observed in AIA 211 Å images separated by two minutes. Figure 7 and the right panel of the movie show contrasted running differences. The left panel of the movie shows the ratios of each current image to a fixed pre-event image observed at 10:56, in which solar rotation was compensated for to the time of the current image. Such ratio images are free from spurious effects in running-difference images caused by subtraction.

An off-limb brightening in Figure 7a facing the far-side flare region denoted by the dot suggests that something already happened as early as 10:58. As Figure 2 indicates, this brightening was due to expansion of high coronal loops caused by an erupting structure, whose liftoff commenced at that time. The EUV wave appears in Figure 7b at 11:00. Its front is indicated in all images by the white arrow parallel to the limb and by the blue bar in the movie. About two minutes later, the second EUV wave front appears (black arrow and red bar). Because it is present in non-subtracted ratio images, it cannot be a subtraction effect.
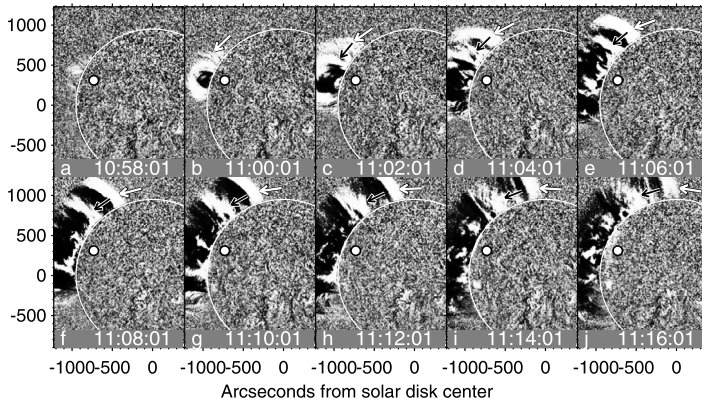
Figure 7 EUV wave propagation along the limb observed in running-difference AIA 211 Å images. The *arrows point* at the first (*white arrow*) and second (*black arrow*) EUV wave fronts. The *white dot* denotes the projected position of the flare site. The *axes* show the distances from solar disk center in arcseconds. The temporal interval between all consecutive images is two minutes.

The northern flanks of the EUV waves are manifest in a bright compression region. The expansion at the southern flank is also detectable, but without a clear leading brightening; it looks like a deepening of an expanding dimming.

We measured the motion of the leading edges of the northern EUV waves at a fixed distance from the limb. The images shown in Figure 7 are sampled uniformly in steps of two minutes. The positions of the white arrow head indicate that the plane-of-the-sky EUV wave speed along the limb was highest initially and then decreased monotonically. For example, the EUV wave speed in Figure 7b (11:00) was ≈ 1000 km s^{-1}, and in Figure 7j (11:16), it decreased to ≈ 560 km s^{-1}. Using a power-law fit to the measurements as described in our articles listed in Section 3, we estimated the onset time for the first EUV wave $t_{01} = 10{:}59{:}04 \pm 15$ seconds. It is more difficult to identify and measure the second EUV wave front. Its probable onset time is $t_{02} = 11{:}02{:}00$ with an uncertainty of about one minute. The measurements are presented and discussed in Section 3.3; the wave speeds are shown in the bottom panel of the movie by the corresponding colors. Both EUV waves decelerated. The deceleration of EUV wave 2 was weaker, which is not obvious from the plot because the strongest-deceleration initial part of the faster EUV wave 1 is not shown.

The EUV waves propagated over a huge area. In Figure 7j, the projected northern flank of EUV wave 1 reached the North Pole, while the southern flank reached the lower edge of the image shown. These moving features apparently had a wave nature.

The expanding wave dome was also observed by STEREO-B (here we focus on the first wave). Figures 8a – 8f present it in combined COR1 and EUVI 195 Å running-difference images. As Plotnikov, Rouillard, and Share (2017) showed, the shape of the wave front was almost an ellipsoid (using the same method, Rouillard *et al.* (2016) made a similar conclusion for a different event). We did not endeavor to outline the wave-dome shape precisely; rather, the black-on-white circles in Figures 8a – 8f approximately reproduce its size. The correspondence between the outlining circles and observations is almost perfect in Figures 8a and 8b. In other panels, thick apparent flanks dominate; they are probably emphasized by deflected streamers and subtraction of the images. Nevertheless, the circles correspond to the faint outermost EUV wave signatures on the solar disk. These circles correspond to a fixed projection of an expanding ellipsoid, whose shape does not change considerably (*cf.*
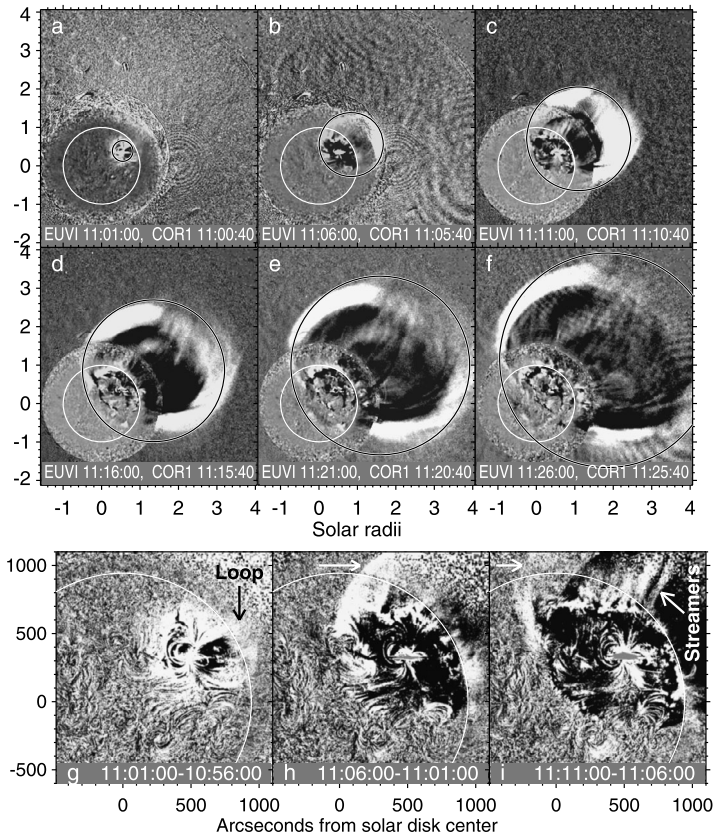
Figure 8 (**a** – **f**) Wave traces observed by STEREO-B/COR1 and EUVI 195 Å running-difference images. The *black-on-white circles* approximately reproduce the extent of the wave front. The *white circles* denote the limb. (**g** – **i**) Wave signatures in enlarged EUVI 195 Å running-difference images shown in panels (**a** – **c**). Panel **g** reveals a set of long loops (*Loop*). The *horizontal arrows* in panels **h** and **i** indicate the EUV wave above the limb. Panel **i** reveals a set of streamer-like structures.

Grechnev *et al.*, 2011c). Thus, the circles correctly reproduce the kinematics of the wave-dome expansion, differing from the highest-speed direction by a nearly constant factor. The measurements are presented in Section 3.3.

Figures 8g – 8i present enlarged EUVI 195 Å running-difference images corresponding to Figures 8a – 8c. Figure 8g reveals a loop-like structure denoted Loop that probably corresponds to the lower part of the loops shown in Figure 6, in which gyrosynchrotron source GS2 was located. Figures 8h and 8i show the EUV wave indicated by the horizontal arrow that corresponds to Figure 7 viewed from a near-Earth vantage point. The lower part of the wave front is tilted with respect to the solar surface. Figure 8i reveals three to five streamer-like structures highlighted by the wave passage.

3.2. Dynamic Radio Spectrum

The dynamic spectrum in Figure 9 presents a radio burst at $10 – 180$ MHz produced by this event. The spectrum was composed from data of the *Nançay Decametric Array* (NDA:
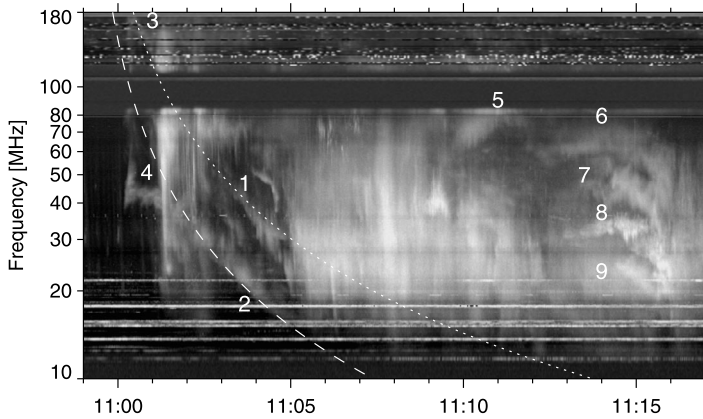
Figure 9 Combined dynamic spectrum of the radio burst composed from the NDA, Sagamore Hill, and San Vito data. The harmonically related *dotted* and *dashed curves* correspond to an expected trajectory of a Type II burst produced by a shock wave with an onset time $t_{01} = 10{:}59{:}04$ in plasma with a density falloff exponent $\mu = 2.75$. *Labels 1, 2,* and *3* denote slowly drifting features that might be possible Type II bands. Non-drifting feature *4* with a reversely drifting *onset* is also a possible Type II-like manifestation. Features *5 – 9*, some with reverse drifts, might also be due to Type II emissions from different structures.

Lecacheux, 2000) at $10 - 80$ MHz and data of the spectrographs at the Sagamore Hill ($80 - 128$ MHz) and San Vito ($128 - 180$ MHz) RSTN stations. The dynamic spectrum presents emissions generated at different locations. The structure of the burst is complex and contains unusual features. Identifying Type II bands that carry information about a shock wave is complicated by a series of stronger Type IIIs (Type VI), a gap between 85 and 110 MHz, and interferences at higher frequencies. To search for indications of possible Type II bands, we plotted their expected trajectories on top of the dynamic spectrum, and by adjusting their parameters, we tried to fit them to the presumed Type II signatures.

The method for calculating a trajectory of a Type II burst is described in our preceding studies (*e.g.* Grechnev *et al.*, 2011b, 2017). We use a power-law density model $n(x) = n_0 (x/h_0)^{-\mu}$ where x is the distance from the eruption center, $n_0 = 5.5 \times 10^8$ cm^{-3} is the density at a distance $h_0 = 100$ Mm (close to the scale height), and μ is the density falloff exponent. This model with appropriate parameters is close to the Saito model (Saito *et al.*, 1970) in the far zone, where the corona is quiet (Section 3.3), and provides higher densities in the near zone (< 260 Mm), where the corona is strongly disturbed by the eruption. Referring to an arbitrary point on the dynamic spectrum at time t_1, we chose a frequency and calculate a corresponding distance x_1 from our density model for the first or second harmonic of the plasma frequency. The wave onset time $t_{01} = 10{:}59{:}04$ was estimated from AIA data. Then, we calculated the Type II trajectory as $x(t) = x_1 [(t - t_{01})/(t - t_1)]^{2/(5 - \mu)}$. A similar approach was used in Section 3.1 to measure the shock-wave kinematics from its signatures in AIA, EUVI, and COR1 images.

The dotted and dashed curves plotted in Figure 9 are harmonically related (2:1) and correspond to an expected trajectory of a Type II burst produced by the first shock wave with an onset time $t_{01} = 10{:}59{:}04$ in plasma with a density falloff exponent $\mu = 2.75$. The trajectories more or less correspond to the slowly drifting features 1 and 2 that are discernible between 11:02:40 and 11:05:00, although their structures are different. The corresponding kinematics is presented in Section 3.3.

The drift rate of the faint higher-frequency feature 3 is somewhat different from the calculated trajectories and can be reproduced using a lower $\mu \approx 2.3$. The source of this emission was probably located in a different structure.

The narrow-band ($\approx 10\%$) feature 4 starts from a fast reverse drift and does not exhibit any drift afterward. Its onset suggests an interaction of a quasi-perpendicular shock on an extended structure with a contact point that rapidly moves to its base. This feature might be caused by a collision of a curved first shock front with a long loop. The collision could excite wave processes responsible for the emission at the plasma frequency in the loop.

A set of unusual features, features $5-9$, is visible between 11:10 and 11:16. They start from reverse drifts, which later turn to the normal direction from high to low frequencies. These are relatively narrow-band features and have a Type III-like structure, similar to Type II bursts. A harmonic counterpart to feature 5 is not detectable. The pairs (6, 8) and (7, 9) are both harmonically related, although the structures of the bands in each pair are not identical. Features $5-9$ might also be due to Type II emission produced by the passage of the shock wave, but the cause of their unusual drifts is not obvious. Their spectral evolution is different from the nondrifting Type II-like bursts presented by Aurass, Vršnak, and Mann (2002) and Aurass (2003) and from inverse-N-like shifts of Type II bands (Grechnev *et al.*, 2011b, 2014a).

As demonstrated in our preceding studies (*e.g.* Grechnev *et al.*, 2015, 2016, 2018), the most probable source of a narrow-band Type II emission is a streamer. The shock crossing the streamer deforms the plasma flow in the vicinity of its current sheet, which induces a flare-like process running along the streamer together with the intersection point. Figures 8c and 8i reveal a set of small streamers visible indeed in an EUVI image at 11:11. The streamers appeared, being blown by a shock front. An oblique shock and compressed plasma flow behind it displace plasma in the streamer along it. The effect is strongest near the shock normal and decreases away from it. Thus, just after the passage of the first shock, an inverse density distribution forms for some time in a portion of the streamer. When the second shock hits the streamer about three minutes later, the intersection point moves upward along the streamer. The instantaneous drift rate reflects the distorted density distribution in the streamer caused by the passage of the preceding shock.

The exact number of the streamers in Figure 8 is not obvious, and neither is the exact number of the sources responsible for features $5-9$ in Figure 9. In addition, the presence of a streamer is a necessary but not sufficient condition to produce Type II emission. With these uncertainties, the number of the streamers roughly corresponds to the response in the dynamic spectrum.

3.3. Summary on Shock-Wave Measurements

The measurements in Sections 3.1 and 3.2 were fitted using power-law distance–time relations: $x(t) \propto (t - t_{01})^{2/(5-\mu)}$. Power-law plots of a shock wave shown on a log–log scale with the origin of the time axis at the wave onset time [t_{01}] are represented by straight lines. In Figure 10 we used the same $t_{01} = 10{:}59{:}04$ in all cases and density falloff exponents $\mu = 2.75$ for the wave signatures in COR1 and EUVI images and dynamic spectrum; $\mu_{AIA} = 2.51$ for EUV wave 1, and $\mu_{AIA} = 2.75$ for EUV wave 2, both running along the limb in AIA images (Figure 7). The plot for EUV wave 2 is conspicuously curved, because it started three minutes after the origin of the plot. This situation demonstrates the sensitivity of the log–log representation to the wave-onset time, which permits estimating it with a high accuracy.

Figure 10 presents the results of the kinematical measurements and their analytic fit by different line styles. Our measurements exactly coincide with the fitting lines because the

Figure 10 Decelerating power-law kinematics of the shock waves measured from different vantage points using different methods. All distances are measured from the eruption center located at 0.84 $R_\odot$. (**a**) Distance–time plots. The *horizontal axis* represents time after the wave onset $t_{01} = 10{:}59{:}04$ in the logarithmic scale. The upper X-axis shows actual times. (**b**) Speed–distance plots. The *symbols* represent our measurements from the images produced by different telescopes. The measurements from the CME catalog are shown by *asterisks* (*C2*) and *diamonds* (*C3*). The *thick bar* represents the shock kinematics corresponding to possible Type II bands outlined in the dynamic spectrum. The *gray squares* denoted PRS represent the measurements from Plotnikov, Rouillard, and Share (2017). The *black lines* of different styles show the analytic fit.
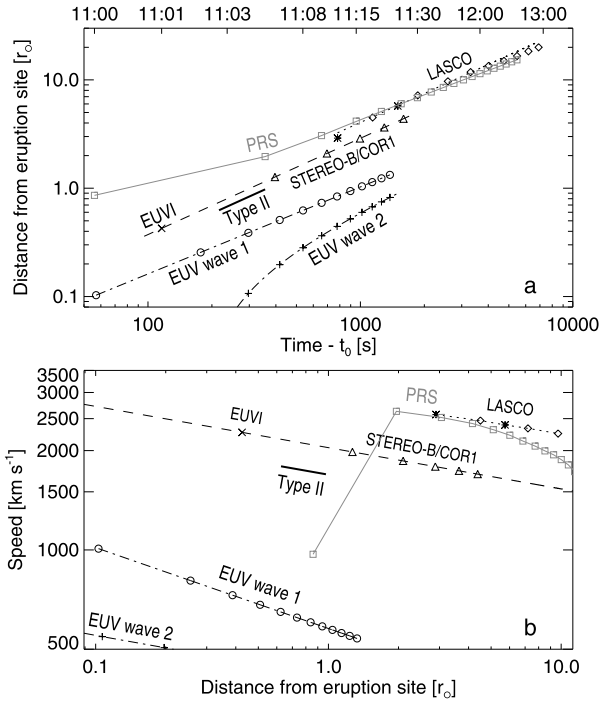
outlining curves in Figures 7, 8, and 9 were calculated analytically and adjusted to the observed wave signatures.

The data from the online CME catalog are shown by asterisks for the measurements from LASCO-C2 images and by diamonds for those from C3 images. The gray squares denoted PRS represent the measurements by Plotnikov, Rouillard, and Share (2017). All of these heliocentric distances are reduced by 0.84 $R_\odot$ to refer to the eruption site (assumed to coincide with the flare position).

The measurements in the CME catalog reveal kinematics close to our results in Figure 10a. The dotted line calculated as our fit of the measurements from EUVI and COR1 images magnified by a factor of 1.4 matches the data from the CME catalog up to 10 $R_\odot$ acceptably well.

All measurements in Figure 10a present similar distance–time histories, except for the curved plot for EUV wave 2 because of its later wave-onset time: $t_{02} > t_{01}$. The difference of 40% between the measurements in the CME catalog from LASCO images and our measurements from STEREO images may be caused by the ellipticity of the shock-wave dome and still more probably by the different techniques that were used. The difference within 20% between the measurements from COR1 images and dynamic radio spectrum can reflect the difference in the shock-wave propagation directions and in plasma densities in coronal structures. The difference between the measurements from AIA and COR1 images reflects a slower motion of the EUV wave across the solar surface and its stronger deceleration with respect to the wave dome that expands away from the Sun (Figures 8b – 8f).

The slopes of the straight fitting lines are $2/(5 - \mu)$, corresponding to $\mu = 2.51$ (the slope of 0.80) for EUV wave 1 and to $\mu = 2.75$ (0.89) for all others. The power-law density model $n(x) = n_0(x/h_0)^{-\mu}$ with $n_0 = 3.75 \times 10^8$ cm^{-3} and $\mu = 2.75$ is close to the Saito

model (Saito *et al.*, 1970) at the latitude of the flare site of $14°$ within $\pm 30\%$ at distances from 260 Mm to 25 $R_\odot$. We recall that we use $n_0 = 5.5 \times 10^8$ cm^{-3} and measure the distance [x] from the eruption center, while the Saito model refers to the heliocentric distance $r = R/R_\odot$, so that $x \approx (r-1)$ $R_\odot$ in the radial direction. Overall, the measurements made using different methods agree reasonably well with an expected propagation of a decelerating blast-wave-like shock in a typical corona.

The expected speed–time dependencies can be obtained by differentiation of distance–time plots: $v(t) \propto (t - t_0)^{2/(5-\mu)-1} = (t - t_0)^{(\mu-3)/(5-\mu)}$. The shock wave propagating in plasma with a density-falloff exponent $\mu < 3$ monotonically decelerates. We only observed decelerating shock waves so far.

For the speed *versus* distance dependence, we obtain from the analytic fit $v(x) \propto x^{(\mu-3)/2}$. In this event, the slope of the speed–distance plots is -0.13 ($\mu = 2.75$) for most shock-wave signatures and -0.23 ($\mu = 2.54$) for EUV wave 1. The latter value corresponds to a stronger deceleration of the slower shock-wave trail on the solar surface in Figure 8, while the whole wave dome expanded self-similarly.

The speed–distance plots are shown in Figure 10b for the distances from 70 Mm to 10 $R_\odot$ from the eruption site. Our measurements from different data agree with each other and with the measurements in the CME catalog within this range. The results of Plotnikov, Rouillard, and Share (2017) within $(1.5-5)$ $R_\odot$ are close to the measurements in the CME catalog, but they show a stronger deceleration at larger distances. However, their first data point is most challenging, with a speed that is about three times slower than expected, whereas our measurements show that the slope persists to much smaller distances. The shock wave did not have any acceleration phase. Instead, the wave started from the fast-mode speed in its origin and decelerated monotonically. We have to conclude that the estimate by Plotnikov, Rouillard, and Share (2017) of the shock-wave speed at its earliest appearance is questionable.

Our results also disagree with Jin *et al.* (2018), who found the shock speed to increase from ≈ 400 km s^{-1} to ≈ 1000 km s^{-1} from the tenth minute since the eruption until the thirtieth minute. This time interval corresponds to the measurements from STEREO-B/COR1 in Figure 10, where the shock speed monotonically decreases from ≈ 2000 km s^{-1} to ≈ 1700 km s^{-1}. A possible cause of the questionable result of Jin *et al.* (2018) might be the difficulty of identifying the shock front from MHD simulations that the authors made. The incorrect behavior of the shock speed probably affected the derived plots. We hope that our results can help in improving the promising method developed by Jin *et al.* (2018).

4. Discussion

4.1. Trapping

One of the challenges of this event is the contrast between the impulsive temporal profiles of the flare HXR emission observed by HEND and long-lasting gyrosynchrotron, HXR, and γ-ray emissions observed from the Earth's direction. Long-duration γ-rays have been observed in the past in a few events and were extensively discussed (see, *e.g.*, Forrest *et al.*, 1985; Akimov *et al.*, 1996; Ryan, 2000; Kurt *et al.*, 2010; Kuznetsov *et al.*, 2011). One possible explanation that was considered was long-term trapping of high-energy protons in closed coronal loops. Microwave bursts often exhibit manifestations of trapping of accelerated electrons (*e.g.* Melnikov and Magun, 1998; Silva, Wang, and Gary, 2000; Kundu *et al.*, 2001). Trapping of protons might also occur (*e.g.* Mandzhavidze and Ramaty, 1992). The
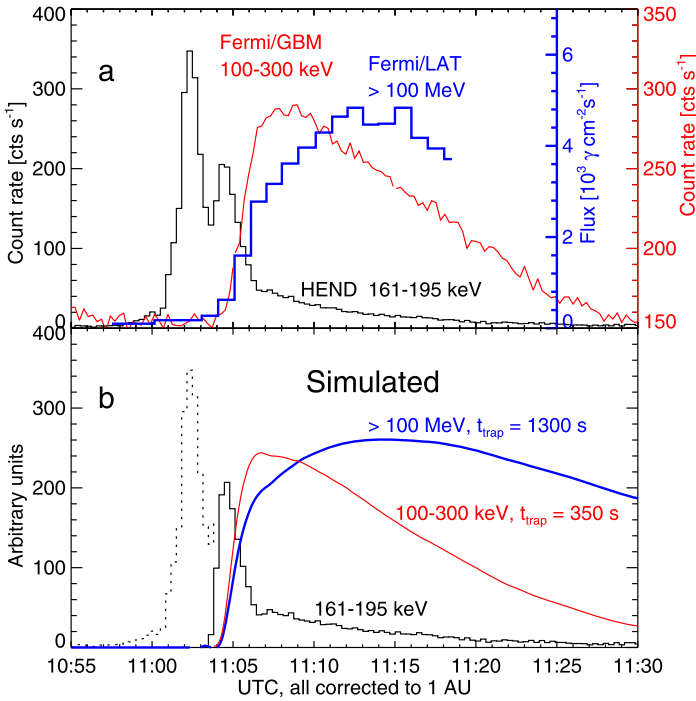
Figure 11 Trapping effect issue. (**a**) Hard emissions actually observed (corresponding to Figure 3): 161 – 195 keV flare hard X-rays (*Mars Odyssey*/HEND, *black*), 100 – 300 keV viewed from the Earth's direction (*Fermi*/GBM, *red*), and > 100 MeV γ-ray burst (*Fermi*/LAT, *thick-blue*). The one-second and four-second time-resolution *Fermi*/GBM data are both summed over 16 seconds for convenience. (**b**) Simulated temporal profiles expected as a result of trapping: the injection function for the second HXR peak [f_{inj}] (*black solid*), actual HXR temporal profile (*black dotted*), and simulated emissions from trapped electrons (*red*) and protons (*thick blue*).

conditions for containing trapped relativistic protons or ions for a long time were summarized by Ryan (2000): low density, low turbulence, and a force-free field. These requirements can be hard to meet for flare loops, but are not critical for lower-density long loops like those in Figure 6 and high-energy protons responsible for the pion-decay emission.

4.1.1. Temporal Profiles

We ask whether the trapping effect can produce the observed long-duration time profiles in response to particle populations that are impulsively injected. Figure 11a reproduces the HXR and γ-ray temporal profiles observed from different vantage points that were presented in Figure 3. As noted, the first HXR peak observed by HEND around 11:02:20 had a very close response in gyrosynchrotron and lower-energy hard X-rays. The main long-duration radio and HXR bursts represent the only response to the second HEND peak around 11:04:30.

At the first step, the second HXR peak needs to be separated from the actual temporal profile. This peak may have been responsible for the long-lasting emissions observed from the Earth's direction. An appropriate shape has a function $\Psi(t, \mu, \tau) = t^{\mu} \exp(-t/\tau)$ (Aschwanden, 2004b) similar to the Landau probability distribution. To separate the second

HXR peak, decomposition of the whole HXR temporal profile is required. We considered three peaks: a minor peak around 11:00:00, the first peak, and the second peak. The decomposition was made by least-squares fitting a linear combination simulating the three peaks to the HXR(t) temporal profile actually observed by HEND. Specifically, we minimized the average value $\overline{Q}$ of the Q quantity defined as

$$Q = \left[\text{HXR}(t) - a_0 \Psi(t, \mu_0, \tau_0) - a_1 \Psi(t, \mu_1, \tau_1) - a_2 \Psi(t, \mu_2, \tau_2) \right]^2.$$

The dotted line in Figure 11b shows the actual HXR temporal profile. The solid line represents the net second peak evaluated from the decomposition.

At the second step, the emissions from trapped particles were simulated following the approach used by Kundu *et al.* (2001). The temporal profiles [$I(t)$] were calculated as

$$I(t) = \int_{-\infty}^{t} \exp\left[-(t - t')/\tau_{\text{trap}} \right] f_{\text{inj}}(t') \, dt',$$

where the extracted second peak found at the first step was used as an injection function [f_{inj}]. The trapping times [τ_{trap}] were adjusted to make the temporal profiles we simulated more or less similar to those actually observed. The results are shown in Figure 11b by the curves whose colors correspond to those of the temporal profiles in Figure 11a. The simulated temporal profiles reproduce the shapes of the bursts actually observed by *Fermi* in HXR and γ-rays acceptably well. We recall that the gyrosynchrotron radio burst was almost identical in shape to the HXR burst (Figure 3). Thus, the simulation demonstrates that the long-lasting HXR and radio emissions observed from the Earth's direction can be well accounted for by trapping of emitting electrons in closed coronal loops.

With the static position of the gyrosynchrotron source, which is shown by NRH to be associated with long closed loops, its origin due to emission from trapped electrons appears to be natural. The same is most likely related to the HXR burst, contrary to the idea of Plotnikov, Rouillard, and Share (2017) about the shock-related origin of accelerated electrons high in the corona and their return to the solar surface along open magnetic structures. In any case, neither electrons nor protons have access to closed loops.

4.1.2. Low-Energy Cutoff of the Electron Spectrum

An additional support for the role of trapping in this event is provided by the spectral information. According to Carley *et al.* (2017), the low-energy cutoff of the electron spectrum in the first peak during $11:01 - 11:04$ was as low as 9 keV. For the main burst between 11:06 and 11:16, Plotnikov, Rouillard, and Share (2017) estimated the low-energy cutoff to be much higher, at 130 keV. We obtained a low-energy cutoff on the order of 100 keV by fitting the gyrosynchrotron spectrum near the maximum of the burst at about 11:08.

The temporal behavior of the electron energy-density spectrum with an increasing low-energy cutoff is really expected in a trap after an initial impulsive injection, $\Delta t_{\text{inj}} \ll \tau_{\text{trap}}$, of electrons with a power-law spectrum (Melrose and Brown, 1976; Metcalf and Alexander, 1999). For the estimate we used the formula from Melrose and Brown (1976) for the turnover energy [$E_{\text{T}} = (3/2 \nu_0 t)^{2/3}$] of the spectrum of fast trapped electrons precipitating into the loss cone because of Coulomb collisions, where $\nu_0 = 5 \times 10^{-9} n_0$ [s^{-1} $(\text{keV})^{3/2}$] and n_0 is the number density of thermal electrons. With an impulsive injection at 11:05 and an ambient density of $n_0 = 6.4 \times 10^8$ cm^{-3}, we estimate [E_{T}] to be 91 keV at 11:08, 44 keV at 11:06, and 216 keV at 11:16. The average turnover energy E_{T} between its values at 11:06 and 11:16 is 130 keV. These expected values for the spectrum of trapped electrons match the

low-energy cutoffs estimated from observations. Note that our simplified simulations and estimates in Section 4.1.1 and the present section do not consider possible changes in the plasma density or other complications.

4.1.3. Trapping of Protons

The temporal profiles and spectral characteristics of the gyrosynchrotron and HXR emissions viewed from the Earth's direction are consistent with a long-term trapping of an electron population that is impulsively injected during the second peak. As our simulation shows, trapping of protons that are responsible for the pion-decay γ-ray emission was also a likely cause of its long duration. The > 100 MeV γ-ray temporal profile obtained in our simulation matches the actual light curve acceptably well. The difference between the durations of the HXR/radio and γ-ray bursts observed from the Earth's direction is much smaller than the difference between either of them and the probable injection function. Plotnikov, Rouillard, and Share (2017) also concluded that accelerated electrons and protons responsible for the long-lasting emissions in this event had a common origin, contrary to the impression of Jin *et al.* (2018) about the drastic difference between the > 100 MeV light curve and all other emissions. The long-lasting π^0-decay emission observed in a few solar events was previously considered by Mandzhavidze and Ramaty (1992) as evidence for trapping of particles in solar flares.

The trapping time has been discussed extensively in the literature (see Aschwanden, 2004a for a review and details). The factors determining the trapping times of electrons and protons in this event need a separate study.

4.1.4. Appearance of Accelerated Particles in a Trap

While the long-term trapping of electrons and protons in the long static set of loops associated with the GS2 source appears to be very probable, this set of loops did not exhibit direct participation in either the flare or CME formation. This circumstance raises the question of how high-energy particles came to these magnetic structures, which are disconnected from the flaring structures and CME.

Most likely, flare-accelerated particles escape into interplanetary space or enter magnetic traps (static or moving) as a result of reconnection processes. Displacement of particles across magnetic-field lines because of drifts or collisions occurs slowly and not efficiently; otherwise, trapping would be exceptional in solar events, contrary to observations.

In our view, the development of an eruption and flare usually starts within a bipolar configuration, which can be a part of a more complex magnetic structure, *e.g.* a magnetic domain of a quadrupole configuration. In this situation, four domains share one null point. The eruptive flux-rope carrying trapped flare-accelerated particles moves toward this point. The passage of the flux-rope at the null inevitably results in local reconnection between its magnetic flux and fluxes belonging to adjacent domains. As a result, both open and closed structures of these domains become filled with energetic particles as well as the cool plasma of the pre-eruptive filament. Related schemes containing a single null point were discussed by Gary and Moore (2004), Meshalkina *et al.* (2009), Masson, Antiochos, and DeVore (2013), Grechnev *et al.* (2013b), and Uralov *et al.* (2014). Stretching a large-scale quadrupole into the solar wind might cause disappearance of the null point. Nevertheless, lateral reconnection between the flux rope and coronal rays also occurs in this situation (*e.g.* Bemporad *et al.*, 2010). The presence of a coronal null in the parent AR 12158 is supported by the S–N–S–N configuration discernible in SDO/HMI magnetograms that were observed one week after the event.

4.2. Position of the Gamma-Ray Source

The > 100 MeV emission centroid position calculated by Ackermann *et al.* (2017) from *Fermi*/LAT data with a 68% error radius of $100''$ is located at the east limb at a latitude of about N41 (Figures 1b and 1c). As noted in Section 2.4, this site and its broad environment were entirely covered by closed magnetic fields. Protons and other charged particles did not have access to this domain from either the flare region or from greater coronal heights along open field lines. On the other hand, the off-limb radio source GS2, which is the most probable candidate for the source of long-duration HXR and γ-ray emissions, was located nearly above the Equator, far away from the *Fermi*/LAT > 100 MeV emission centroid position. No other candidate for the source of the long-duration burst was found. The difference between the expected position of the γ-ray source and the > 100 MeV emission centroid position computed by Ackermann *et al.* (2017) encourages considering its possible causes.

The centroid position of the observed γ-ray emission can be due to superposition of a few different sources. For example, high-energy cosmic rays arriving from outside the solar system can produce cascades of secondary particles and γ-rays in the solar corona. Next, intense fluxes of energetic particles and emissions from the flare site can interact with dense streamers, producing secondaries, in particular γ-rays. Furthermore, the expanding CME is a low-density but huge target for both extra-solar cosmic rays and energetic flare emissions. Kahler and Ragot (2008) showed a possibility for high-energy γ-rays to be produced even in interactions between SEPs and solar wind. All of these presumable processes might influence the centroid position, while their effects are mostly expected in the lowest-energy part of the spectrum observed by *Fermi*/LAT.

Proceeding from these considerations, we attempted to find a possible dependence of the *Fermi*/LAT emission centroid position on the low-energy threshold. We analyzed the Level 1 Photon File available at fermi.gsfc.nasa.gov/ssc/data/ that included the SOL2014-09-01 event. The file presents the time, energy, and position (arrival direction) measured for each individual γ-ray photon out of numerous discrete sources detected during the observational interval recorded in the file. We calculated the emission centroid positions from these data, eliminating the γ-ray photons with energies below a given threshold E_{min}. We did not reproduce the sophisticated method used by Ackermann *et al.* (2017) to reach the highest accuracy, making the calculations in the same way for each E_{min}.

The centroid position that we found with $E_{min} = 100$ MeV was close to the result of Ackermann *et al.* (2017). Then we increased E_{min} in steps of 50 MeV and found a monotonic displacement of the centroid position along the limb toward the Southeast. The increase of E_{min} from 100 MeV to 300 MeV shifted it by $\approx 30°$ toward the radio source GS2. Our experiment shows that the effects described in this section can account for the discrepancy between the expected position of the source and the centroid position that is actually measured. This issue needs further study.

The energy dependence of the γ-ray centroid position is difficult to reconcile with the scenario proposed by Jin *et al.* (2018). We also recall the similarity of simulated HXR and γ-ray temporal profiles emitted from the trap after the same impulsive injection with those actually observed (Section 4.1.1). To fit within the scenario by Jin *et al.* (2018), accelerated electrons and protons of a common origin have to be separated and enter different structures to emit at the positions located far away from each other. Electrons have to come to the off-limb source GS2, while protons have to precipitate at the on-disk γ-ray centroid position. It seems difficult to realize this separation. GS2 appears to be a more probable source of both HXR and γ-ray emissions. According to Hudson (2018), the column density nL required for the effective interaction of high-energy protons with ambient plasma can be accumulated

in their numerous flights in a coronal trap (large L) and need not be due to a large n in the photosphere.

4.3. Histories and Possible Roles of Shock Waves

4.3.1. Excitation and Evolution of Shock Waves

As shown in our preceding case studies of shock-wave histories in a dozen events, the only initial shock-wave excitation scenario observed in flare-related eruptions is the impulsive-piston mechanism (Grechnev *et al.*, 2018). Here, a sharply erupting flux rope produces a strong MHD disturbance, whose initial speed is determined by the fast-mode speed V_{fast}, which is high in active regions ($V_{fast} > 1000$ km s^{-1}). Away from the eruption site, the V_{fast} in the environment decreases both upwards and laterally, reaching ≈ 200 km s^{-1} above the quiet Sun. When a high-speed disturbance enters the lower-V_{fast} environment, its pro-file steepens, and the disturbance rapidly becomes a shock wave. The shock formation is governed by the maximum acceleration of the eruption and the V_{fast} falloff away from the eruption site, occurring presumably in $10 - 100$ seconds (Afanasyev, Uralov, and Grechnev, 2013). Then the shock wave propagates quasi-freely up to considerable distances from the Sun like a decelerating blast wave. Being highly efficient, the impulsive-piston scenario ini-tially precedes the bow-shock excitation by the outer surface of a CME that is only possible when it becomes super-Alfvénic. The change to the bow-shock regime occurs later, if the trailing CME is fast (Grechnev *et al.*, 2015, 2017).

The onset time of a shock wave excited in this way falls in the acceleration phase of the responsible eruption, *i.e.* during the rise phase of an HXR (microwave) burst. In a number of events, the acceleration of an eruption and shock onset time advanced the bursts by about two minutes (*e.g.* Grechnev *et al.*, 2011b, 2013a, 2015, 2016, 2018). In several events, two shock waves excited within a few minutes by different eruptions were observed to follow each other. As shown in the articles listed, flare-generated shock waves are unlikely.

These conclusions shed light on the event in question. The presence of two EUV waves with onset times at 10:59:04 and 11:02:00 indicates excitation of two shock waves one after another by two presumable eruptions responsible for the HXR peaks observed by HEND around 11:02:20 and 11:04:30. Note that two bow shocks cannot be driven by a single CME. Most likely, two shock waves following each other eventually merge into a single, stronger shock propagating nearly radially (Grechnev *et al.*, 2011b, 2013a, 2017). We do not have sufficient data about this process in our event and focus here on the first shock wave.

In the power-law description of a shock wave, the plasma density and wave speed become infinite at the origin ($t = 0$, $x = 0$). This singularity is not important because the shock forms at a certain distance from the origin, while the initial wave speed is determined by the fast-mode speed. From Figure 10b, the initial shock-wave speed in the radial direction was about 3500 km s^{-1}, which is a normal value for V_{fast} in an active region. The kinematical histories of the shock waves at least up to 10 R$_\odot$ exhibit an overall quantitative agreement with the expected evolution outlined in the preceding paragraphs. Here we did not follow the shock-wave evolution in coronagraph images; the close correspondence of the calculated wave fronts to their signatures in the images and agreement with the measurements in the CME catalog has previously been shown for several events (Grechnev *et al.*, 2011b,c, 2014a, 2015, 2016, 2017, 2018).

There is no reason to presume the 1 September 2014 event to be exceptional. The shock-wave excitation and subsequent evolution appear to correspond to the impulsive-piston sce-nario outlined above. This shock-wave history is more complex than the bow-shock excita-tion by a super-Alfvénic piston alone, being, in fact, a combination of known scenarios (see,

e.g., Vršnak and Cliver, 2008). Missing this circumstance can result in incorrect estimates and inadequate conclusions.

In this respect, a question remains about the first estimate by Plotnikov, Rouillard, and Share (2017) of the shock-wave speed, which is an outlier in Figure 10. It follows from the description of the method by Rouillard *et al.* (2016) that the speed is calculated from the spatial separation of successive shock-front ellipsoids obtained in the three-dimensional reconstruction, which appears to be justified. However, this method does not provide an estimate for the first and last speeds. This is probably the key to the problem, which seems to be systematic; the initial speeds also seem to be strongly underestimated for the three different events addressed in these articles. Another possible source of an additional error can be an apparent temporal difference between the first SDO/AIA images and a STEREO/EUVI or COR1 image presented in the articles; a combination of the highest shock speed with the smallest size of its front can result in a large error for the initial point.

On the other hand, we emphasize the importance of a particular result of Rouillard *et al.* (2016) and Plotnikov, Rouillard, and Share (2017) about the ellipsoidal shape of the shock front, which in fact confirms the scenario outlined above. A similar shape of the shock-wave front was predicted by Grechnev *et al.* (2011b), in contrast to the bow shape with a Mach cone considered by Ontiveros and Vourlidas (2009). The reason is a three-dimensional expansion of the CME body (*cf.* Vršnak and Cliver, 2008). Our expectations were later confirmed in studies by Kwon, Zhang, and Olmedo (2014) and Kwon, Zhang, and Vourlidas (2015). Elaboration of the shock-front reconstruction method by Rouillard *et al.* (2016) promises further progress in understanding coronal shock waves.

4.3.2. Possible Particle Reacceleration by an Oblique Shock Wave

As Hudson (2018) noted, our event resembles the SOL1969-03-30 event addressed by Frost and Dennis (1971), who considered the HXR emission observed in that event as evidence for two-stage electron acceleration (initially assumed by Wild, Smerd, and Weiss, 1963). The first-stage acceleration was associated with flare processes, while the shock front could be responsible for the second-stage acceleration. The two-stage acceleration can also apply to protons. Observations of the SOL2014-09-01 event might shed light on this issue.

An additional acceleration of high-energy protons in a static magnetic trap could be caused by a fast magnetosonic shock wave, whose front positions are shown in Figure 7. The shock front propagating with the phase velocity V_{sh} intersects a part of the magnetic trap at an angle $[\psi]$ to the magnetic field $[B]$. An important characteristic here is the velocity $[u]$ of the intersection point between a magnetic-field line and the shock-front surface: $u = V_{sh} \tan \psi$. We briefly discuss the case of an oblique shock wave with $u < c$.

High-energy particles with gyroradii considerably exceeding the shock-front thickness change their energy by virtue of the following effects. The first effect results from the first adiabatic-invariant $p_\perp^2/B$ conservation, where $p_\perp$ is a component of the particle momentum perpendicular to the magnetic field $p = mV/(1 - V^2/c^2)^{1/2}$, m is the rest mass of the particle, and V is its velocity. Particles that are initially upstream of the shock, with pitch angles in the loss cone, pass into the downstream region of a stronger magnetic field and increase their transverse kinetic energy $K_\perp$. On the other hand, their longitudinal kinetic energy $K_\parallel$ also changes because of the second effect of bouncing particles against the moving magnetic mirror of the shock front. The change $\Delta E = \Delta K$ in the total energy $E = mc^2 + K_\perp + K_\parallel = mc^2 + K$ depends on the initial pitch angle, velocity u, and ψ, and it can be either positive or negative.

The growth of the total energy due to the increasing $K_\parallel$ is most conspicuous for particles reflected upstream after their interaction with the shock. In this case, $\Delta K =$

$2up'/(1-u^2/c^2)^{1/2}$ (Webb, Axford, and Terasawa, 1983), where p' is a gyrophase-averaged value of the particle's momentum projection on the shock-front surface in the frame moving along the front with the velocity $[u]$. In the nonrelativistic limit ($u^2/c^2 \ll 1$), $\Delta K = 2u(2mK')^{1/2}/(1-u^2/c^2)^{1/2}$, where $K' = (p')^2/2m$. The particles gain energy owing to the reflection from a moving magnetic mirror, *i.e.* the shock front for upstream particles with sufficiently large pitch angles. We are only interested in a qualitative analysis of the particle behavior in a magnetic trap through which a shock wave passes. Therefore, we replace the last relation with a rough proportionality $\Delta K_{\parallel} \propto K_{\parallel}^{1/2}$. The higher the energy of a particle, the larger the increase in its energy and velocity per each reflection. The higher the particle velocity, the more reflections it has in bouncing between the moving shock front and the base of the magnetic trap. Thus, particle acceleration is accompanied by flattening of the initial energy spectrum.

After the shock-front passage, the magnetic-loop trap compresses and displaces following the wave. The magnetic field strength B increases. Then the trap returns to its initial condition, and B decreases to the initial value. With a decreasing B, the transverse energy $K_{\perp}$ of each particle decreases approximately as much as it increased in the interaction with the shock front because of the first adiabatic-invariant conservation. However, the longitudinal energy $K_{\parallel}$ accumulated in the reflections from the shock front is retained, as well as the energy-spectrum flattening. This conclusion seems to correspond to the observations.

The completeness of this scheme for the proton acceleration in a trap is open to question. The acceleration mechanism based on reflections from the magnetic mirror in the shock front leads to an increase in the longitudinal energies of particles. This suggests a decrease in their pitch angles and possible precipitation into the loss cone of the magnetic trap. Precipitation of a fraction of energetic particles into the bases of the trap is expected to occur in the course of the oblique-shock propagation through a trap. This phenomenon might be manifested in the long-duration tail of the HXR emission observed by HEND in Figure 3a. Precipitation may be reduced because of the electric field due to the charge separation in the front of a collisionless shock wave. Such an electric field increases the transverse energy of reflected protons to prolong their confinement in the trap.

5. Summary and Conclusions

A combined analysis of observations of the far-side SOL2014-09-01 event from different vantage points has revealed the following circumstances:

  i) The liftoff of a hot (about 10 MK) blob has been detected, which probably was an erupting flux rope. The blob rose radially and became the CME core.
 ii) Unocculted flare emission consisted of two HXR peaks with similar spectra separated by 2.5 minutes.
iii) Each of the two flare peaks was preceded by the appearance of a shock wave by two to three minutes.
 iv) The first HXR peak was manifested in a static off-limb gyrosynchrotron radio source of a corresponding duration and spectrum.
  v) The second HXR peak gave rise to a different static off-limb gyrosynchrotron radio source of a considerably longer duration and harder spectrum. This radio source was located in a system of long loops.
 vi) The long-duration gyrosynchrotron burst from the second source was almost identical in shape to the HXR burst observed from the Earth's direction and rather similar to

the > 100 MeV γ-ray burst. All of these emissions could be produced by populations of electrons and protons injected into the long loops during the second flare burst and trapped there for a long time.

vii) The harder spectrum of the long-duration burst relative to the injection could be due to reacceleration of the particles trapped in closed loops by the second shock wave.

viii) The observations indicate that the sources of the gyrosynchrotron, HXR, and γ-ray emissions had a common location. It was considerably displaced with respect to the > 100 MeV γ-ray emission centroid position. A probable key to the discrepancy is a contribution of γ-rays coming from high coronal structures and possibly the CME. The role of non-solar high-energy cosmic rays is not excluded.

These findings can be reconciled within the following scenario. Two sharp eruptions probably occurred in AR 12158 with a separation of about 2.5 minutes. Each eruption impulsively excited a blast-wave-like shock on the one hand, and resulted in strong particle acceleration in the flare site on the other hand. Manifestations of the first flare peak were observed from the Earth's direction as an impulsive brightening of the arcade top. During the second peak, accelerated electrons and protons were injected into long loops, where they become trapped for a long time. The second shock wave possibly hit these loops obliquely, which resulted in reacceleration of trapped flare-accelerated electrons and protons. This presumable episode was not crucial; the long-duration gyrosynchrotron, hard X-ray, and γ-ray emissions were radiated from trapped particles, while reacceleration hardened their spectra. A presumable scenario with a shock-acceleration of particles high in the corona and their return to the solar surface along open magnetic structures meets basic difficulties and is not confirmed by observations.

The region of trapped electrons and protons was located above the limb. Its connection to the Earth-facing solar surface near the Equator is not excluded, but does not seem to be necessary.

While our analysis sheds additional light on this event, a number of issues remain to be addressed. We hope that our results will highlight possible ways for future studies.

Disclosure of Potential Conflicts of Interest　　The authors declare that they have no conflicts of interest.

References

Ackermann, M., Allafort, A., Baldini, L., Barbiellini, G., Bastieri, D., Bellazzini, R., Bissaldi, E., Bonino, R., Bottacini, E., Bregeon, J., *et al.*: 2017, Fermi-LAT observations of high-energy behind-the-limb solar flares. *Astrophys. J.* **835**, 219. DOI. ADS.

Afanasyev, A.N., Uralov, A.M., Grechnev, V.V.: 2013, Propagation of a fast magnetoacoustic shock wave in the magnetosphere of an active region. *Astron. Rep.* **57**, 594. DOI. ADS.

Akimov, V.V., Ambrož, P., Belov, A.V., Berlicki, A., Chertok, I.M., Karlický, M., Kurt, V.G., Leikov, N.G., Litvinenko, Y.E., Magun, A., Minko-Wasiluk, A., Rompolt, B., Somov, B.V.: 1996, Evidence for prolonged acceleration based on a detailed analysis of the long-duration solar gamma-ray flare of June 15, 1991. *Solar Phys.* **166**, 107. DOI. ADS.

Aptekar, R.L., Frederiks, D.D., Golenetskii, S.V., Ilynskii, V.N., Mazets, E.P., Panov, V.N., Sokolova, Z.J., Terekhov, M.M., Sheshin, L.O., Cline, T.L., Stilwell, D.E.: 1995, Konus-W gamma-ray burst experiment for the GGS wind spacecraft. *Space Sci. Rev.* **71**, 265. DOI. ADS.

Aschwanden, M.J.: 2004a, *Physics of the Solar Corona. An Introduction*, Praxis Publishing Ltd., Chichester. Chapter 12. ADS.

Aschwanden, M.J.: 2004b, Pulsed particle injection in a reconnection-driven dynamic trap model in solar flares. *Astrophys. J.* **608**, 554. DOI. ADS.

Aschwanden, M.J.: 2012, GeV particle acceleration in solar flares and ground level enhancement (GLE) events. *Space Sci. Rev.* **171**, 3. DOI. ADS.

Atwood, W.B., Abdo, A.A., Ackermann, M., Althouse, W., Anderson, B., Axelsson, M., Baldini, L., Ballet, J., Band, D.L., Barbiellini, G., *et al.*: 2009, The Large Area Telescope on the Fermi Gamma-Ray Space Telescope mission. *Astrophys. J.* **697**, 1071. DOI. ADS.

Aurass, H.: 2003, Solar radio bursts after Yohkoh and SOHO. *Hvar Obs. Bull.* **27**, 103. ADS.

Aurass, H., Vršnak, B., Mann, G.: 2002, Shock-excited radio burst from reconnection outflow jet? *Astron. Astrophys.* **384**, 273. DOI. ADS.

Bemporad, A., Soenen, A., Jacobs, C., Landini, F., Poedts, S.: 2010, Side magnetic reconnections induced by coronal mass ejections: observations and simulations. *Astrophys. J.* **718**, 251. DOI. ADS.

Berghmans, D., Hochedez, J.F., Defise, J.M., Lecat, J.H., Nicula, B., Slemzin, V., Lawrence, G., Katsyiannis, A.C., van der Linden, R., Zhukov, A., *et al.*: 2006, SWAP onboard PROBA 2, a new EUV imager for solar monitoring. *Adv. Space Res.* **38**, 1807. DOI. ADS.

Boynton, W.V., Feldman, W.C., Mitrofanov, I.G., Evans, L.G., Reedy, R.C., Squyres, S.W., Starr, R., Trombka, J.I., D'Uston, C., Arnold, J.R., *et al.*: 2004, The Mars Odyssey gamma-ray spectrometer instrument suite. *Space Sci. Rev.* **110**, 37. DOI. ADS.

Brueckner, G.E., Howard, R.A., Koomen, M.J., Korendyke, C.M., Michels, D.J., Moses, J.D., Socker, D.G., Dere, K.P., Lamy, P.L., Llebaria, A., *et al.*: 1995, The Large Angle Spectroscopic Coronagraph (LASCO). *Solar Phys.* **162**, 357. DOI. ADS.

Carley, E.P., Vilmer, N., Simões, P.J.A., Ó Fearraigh, B.: 2017, Estimation of a coronal mass ejection magnetic field strength using radio observations of gyrosynchrotron radiation. *Astron. Astrophys.* **608**, A137. DOI. ADS.

Cheng, X., Zhang, J., Liu, Y., Ding, M.D.: 2011, Observing flux rope formation during the impulsive phase of a solar eruption. *Astrophys. J. Lett.* **732**, L25. DOI. ADS.

Chertok, I.M., Belov, A.V., Grechnev, V.V.: 2015, A simple way to estimate the soft X-ray class of far-side solar flares observed with STEREO/EUVI. *Solar Phys.* **290**, 1947. DOI. ADS.

Chupp, E.L., Ryan, J.M.: 2009, High energy neutron and pion-decay gamma-ray emissions from solar flares. *Res. Astron. Astrophys.* **9**, 11. DOI. ADS.

Cliver, E.W., Kahler, S.W., Vestrand, W.T.: 1993, On the origin of gamma-ray emission from the behind-the-limb flare on 29 September 1989. In: Leahy, D.A., Hicks, R.B., Venkatesan, D. (eds.) *Internat. Cosmic Ray Conf.* **3**, World Scientific, Singapore, 91. ADS.

Dulk, G.A.: 1985, Radio emission from the sun and stars. *Annu. Rev. Astron. Astrophys.* **23**, 169. DOI. ADS.

Dulk, G.A., Marsh, K.A.: 1982, Simplified expressions for the gyrosynchrotron radiation from mildly relativistic, nonthermal and thermal electrons. *Astrophys. J.* **259**, 350. DOI. ADS.

Forrest, D.J., Vestrand, W.T., Chupp, E.L., Rieger, E., Cooper, J.F., Share, G.H.: 1985, Neutral pion production in solar flares. In: *Internat. Cosmic Ray Conf.* **4**, NASA/GSFC, Greenbelt, 146. ADS.

Frost, K.J., Dennis, B.R.: 1971, Evidence from hard X-rays for two-stage particle acceleration in a solar flare. *Astrophys. J.* **165**, 655. DOI. ADS.

Gary, G.A., Moore, R.L.: 2004, Eruption of a multiple-turn helical magnetic flux tube in a large flare: evidence for external and internal reconnection that fits the breakout model of solar magnetic eruptions. *Astrophys. J.* **611**, 545. DOI. ADS.

Grechnev, V.V., Uralov, A.M., Slemzin, V.A., Chertok, I.M., Kuzmenko, I.V., Shibasaki, K.: 2008a, Absorption phenomena and a probable blast wave in the 13 July 2004 eruptive event. *Solar Phys.* **253**, 263. DOI. ADS.

Grechnev, V.V., Kurt, V.G., Chertok, I.M., Uralov, A.M., Nakajima, H., Altyntsev, A.T., Belov, A.V., Yushkov, B.Y., Kuznetsov, S.N., Kashapova, L.K., Meshalkina, N.S., Prestage, N.P.: 2008b, An extreme solar event of 20 January 2005: properties of the flare and the origin of energetic particles. *Solar Phys.* **252**, 149. DOI. ADS.

Grechnev, V.V., Kuzmenko, I.V., Chertok, I.M., Uralov, A.M.: 2011a, Solar flare-related eruptions followed by long-lasting occultation of the emission in the He II 304 Å line and in microwaves. *Astron. Rep.* **55**, 637. DOI. ADS.

Grechnev, V.V., Uralov, A.M., Chertok, I.M., Kuzmenko, I.V., Afanasyev, A.N., Meshalkina, N.S., Kalashnikov, S.S., Kubo, Y.: 2011b, Coronal shock waves, EUV waves, and their relation to CMEs. I. Reconciliation of "EIT waves", type II radio bursts, and leading edges of CMEs. *Solar Phys.* **273**, 433. DOI. ADS.

Grechnev, V.V., Afanasyev, A.N., Uralov, A.M., Chertok, I.M., Eselevich, M.V., Eselevich, V.G., Rudenko, G.V., Kubo, Y.: 2011c, Coronal shock waves, EUV waves, and their relation to CMEs. III. Shock-associated CME/EUV wave in an event with a two-component EUV transient. *Solar Phys.* **273**, 461. DOI. ADS.

Grechnev, V.V., Kiselev, V.I., Uralov, A.M., Meshalkina, N.S., Kochanov, A.A.: 2013a, An updated view of solar eruptive flares and the development of shocks and CMEs: history of the 2006 December 13 GLE-productive extreme event. *Publ. Astron. Soc. Japan* **65**, S9. DOI. ADS.

Grechnev, V.V., Kuz'menko, I.V., Uralov, A.M., Chertok, I.M., Kochanov, A.A.: 2013b, Microwave negative bursts as indications of reconnection between eruptive filaments and a large-scale coronal magnetic environment. *Publ. Astron. Soc. Japan* **65**, S10. DOI. ADS.

Grechnev, V.V., Uralov, A.M., Chertok, I.M., Slemzin, V.A., Filippov, B.P., Egorov, Y.I., Fainshtein, V.G., Afanasyev, A.N., Prestage, N.P., Temmer, M.: 2014a, A challenging solar eruptive event of 18 November 2003 and the causes of the 20 November geomagnetic superstorm. II. CMEs, shock waves, and drifting radio bursts. *Solar Phys.* **289**, 1279. DOI. ADS.

Grechnev, V.V., Uralov, A.M., Slemzin, V.A., Chertok, I.M., Filippov, B.P., Rudenko, G.V., Temmer, M.: 2014b, A challenging solar eruptive event of 18 November 2003 and the causes of the 20 November geomagnetic superstorm. I. Unusual history of an eruptive filament. *Solar Phys.* **289**, 289. DOI. ADS.

Grechnev, V.V., Uralov, A.M., Kuzmenko, I.V., Kochanov, A.A., Chertok, I.M., Kalashnikov, S.S.: 2015, Responsibility of a filament eruption for the initiation of a flare, CME, and blast wave, and its possible transformation into a bow shock. *Solar Phys.* **290**, 129. DOI. ADS.

Grechnev, V.V., Uralov, A.M., Kochanov, A.A., Kuzmenko, I.V., Prosovetsky, D.V., Egorov, Y.I., Fainshtein, V.G., Kashapova, L.K.: 2016, A tiny eruptive filament as a flux-rope progenitor and driver of a large-scale CME and wave. *Solar Phys.* **291**, 1173. DOI. ADS.

Grechnev, V.V., Kiselev, V.I., Uralov, A.M., Klein, K.-L., Kochanov, A.A.: 2017, The 26 December 2001 solar eruptive event responsible for GLE63: III. CME, shock waves, and energetic particles. *Solar Phys.* **292**, 102. DOI. ADS.

Grechnev, V.V., Lesovoi, S.V., Kochanov, A.A., Uralov, A.M., Altyntsev, A.T., Gubin, A.V., Zhdanov, D.A., Ivanov, E.F., Smolkov, G.Y., Kashapova, L.K.: 2018, Multi-instrument view on solar eruptive events observed with the Siberian radioheliograph: from detection of small jets up to development of a shock wave and CME. *J. Atmos. Solar-Terr. Phys.* **174**, 46. DOI. ADS.

Guidice, D.A.: 1979, Sagamore Hill Radio Observatory, Air Force Geophysics Laboratory, Hanscom Air Force Base, Massachusetts 01731. Report. *Bull. Am. Astron. Soc.* **11**, 311. ADS.

Guidice, D.A., Cliver, E.W., Barron, W.R., Kahler, S.: 1981, The air force RSTN system. *Bull. Am. Astron. Soc.* **13**, 553. ADS.

Howard, R.A., Moses, J.D., Vourlidas, A., Newmark, J.S., Socker, D.G., Plunkett, S.P., Korendyke, C.M., Cook, J.W., Hurley, A., Davila, J.M., *et al.*: 2008, Sun Earth connection coronal and heliospheric investigation (SECCHI). *Space Sci. Rev.* **136**, 67. DOI. ADS.

Hudson, H.S.: 2018, The relationship between long-duration gamma-ray flares and solar cosmic rays. In: Foullon, C., Malandraki, O.E. (eds.) *Space Weather of the Heliosphere: Processes and Forecasts*, *IAU Symp.*, **335**, Cambridge University Press, Cambridge, 49. DOI. ADS.

Hudson, H., Ryan, J.: 1995, High-energy particles in solar flares. *Annu. Rev. Astron. Astrophys.* **33**, 239. DOI. ADS.

Jin, M., Petrosian, V., Liu, W., Nitta, N.V., Omodei, N., Rubio da Costa, F., Effenberger, F., Li, G., Pesce-Rollins, M., Allafort, A., Manchester, W. IV: 2018, Data-driven simulations of magnetic connectivity in behind-the-limb γ-ray flares and associated coronal mass ejections. *Astrophys. J.*, accepted. arXiv

Kahler, S.W.: 2001, Origin and properties of solar energetic particles in space. In: Song, P., Singer, H.J., Siscoe, G.L. (eds.) *Space Weather*, *Geophys. Mono. Ser.* **125**, AGU, Washington, 109. DOI. ADS.

Kahler, S.W., Ragot, B.R.: 2008, Remote sensing of gamma-ray emission from solar energetic proton interactions with the solar wind. *Astrophys. J.* **675**, 846. DOI. ADS.

Kaiser, M.L., Kucera, T.A., Davila, J.M., St. Cyr, O.C., Guhathakurta, M., Christian, E.: 2008, The STEREO mission: an introduction. *Space Sci. Rev.* **136**, 5. DOI. ADS.

Kallenrode, M.-B.: 2003, Current views on impulsive and gradual solar energetic particle events. *J. Phys. G, Nucl. Part. Phys.* **29**, 965. ADS.

Kerdraon, A., Delouis, J.-M.: 1997, The Nançay radioheliograph. In: Trottet, G. (ed.) *Coronal Physics from Radio and Space Observations*, *Lecture Notes in Physics* **483**, Springer, Berlin, 192. DOI. ADS.

Kiplinger, A.L.: 1995, Comparative studies of hard X-ray spectral evolution in solar flares with high-energy proton events observed at Earth. *Astrophys. J.* **453**, 973. DOI. ADS.

Kochanov, A.A., Anfinogentov, S.A., Prosovetsky, D.V., Rudenko, G.V., Grechnev, V.V.: 2013, Imaging of the solar atmosphere by the Siberian solar radio telescope at 5.7 GHz with an enhanced dynamic range. *Publ. Astron. Soc. Japan* **65**, S19. DOI. ADS.

Kundu, M.R., White, S.M., Shibasaki, K., Sakurai, T., Grechnev, V.V.: 2001, Spatial structure of simple spiky bursts at microwave/millimeter wavelengths. *Astrophys. J.* **547**, 1090. DOI. ADS.

Kurt, V.G., Yushkov, B.Y., Kudela, K., Galkin, V.I.: 2010, High-energy gamma radiation of solar flares as an indicator of acceleration of energetic protons. *Cosm. Res.* **48**, 70. DOI. ADS.

Kuzmenko, I.V., Grechnev, V.V.: 2017, Development and parameters of a non-self-similar CME caused by the eruption of a quiescent prominence. *Solar Phys.* **292**, 143. DOI.

Kuznetsov, A.A., Nita, G.M., Fleishman, G.D.: 2011, Three-dimensional simulations of gyrosynchrotron emission from mildly anisotropic nonuniform electron distributions in symmetric magnetic loops. *Astrophys. J.* **742**, 87. DOI. ADS.

Kuznetsov, S.N., Kurt, V.G., Yushkov, B.Y., Kudela, K., Galkin, V.I.: 2011, Gamma-ray and high-energy-neutron measurements on CORONAS-F during the solar flare of 28 October 2003. *Solar Phys.* **268**, 175. DOI. ADS.

Kwon, R.-Y., Zhang, J., Olmedo, O.: 2014, New insights into the physical nature of coronal mass ejections and associated shock waves within the framework of the three-dimensional structure. *Astrophys. J.* **794**, 148. DOI. ADS.

Kwon, R.-Y., Zhang, J., Vourlidas, A.: 2015, Are halo-like solar coronal mass ejections merely a matter of geometric projection effects? *Astrophys. J. Lett.* **799**, L29. DOI. ADS.

Lecacheux, A.: 2000, The Nançay decameter array: a useful step towards giant, new generation radio telescopes for long wavelength radio astronomy. In: Stone, R.G., Weiler, K.W., Goldstein, M.L., Bougerot, J.-L. (eds.) *Radio Astronomy at Long Wavelengths, Tutorials and Reviews from an AGU Chapman Conference*, *Geophys. Mono. Ser.* **119**, AGU, Washington, 321. DOI. ADS.

Lemen, J.R., Title, A.M., Akin, D.J., Boerner, P.F., Chou, C., Drake, J.F., Duncan, D.W., Edwards, C.G., Friedlaender, F.M., Heyman, G.F., *et al.*: 2012, The Atmospheric Imaging Assembly (AIA) on the Solar Dynamics Observatory (SDO). *Solar Phys.* **275**, 17. DOI. ADS.

Livshits, M.A., Belov, A.V.: 2004, When and where are solar cosmic rays accelerated most efficiently? *Astron. Rep.* **48**, 665. DOI. ADS.

Livshits, M.A., Zimovets, I.V., Golovin, D.V., Nizamov, B.A., Vybornov, V.I., Mitrofanov, I.G., Kozyrev, A.S., Litvak, M.L., Sanin, A.B., Tretyakov, V.I.: 2017, Catalog of hard X-ray solar flares detected with Mars Odyssey/HEND from the Mars orbit in 2001-2016. *Astron. Rep.* **61**, 791. DOI. ADS.

Mandzhavidze, N., Ramaty, R.: 1992, Gamma rays from pion decay – evidence for long-term trapping of particles in solar flares. *Astrophys. J. Lett.* **396**, L111. DOI. ADS.

Masson, S., Antiochos, S.K., DeVore, C.R.: 2013, A model for the escape of solar-flare-accelerated particles. *Astrophys. J.* **771**, 82. DOI. ADS.

Meegan, C., Lichti, G., Bhat, P.N., Bissaldi, E., Briggs, M.S., Connaughton, V., Diehl, R., Fishman, G., Greiner, J., Hoover, A.S., *et al.*: 2009, The Fermi gamma-ray burst monitor. *Astrophys. J.* **702**, 791. DOI. ADS.

Melnikov, V.F., Magun, A.: 1998, Spectral flattening during solar radio bursts at cm–mm wavelengths and the dynamics of energetic electrons in a flare loop. *Solar Phys.* **178**, 153. DOI. ADS.

Melrose, D.B., Brown, J.C.: 1976, Precipitation in trap models for solar hard X-ray bursts. *Mon. Not. Roy. Astron. Soc.* **176**, 15. DOI. ADS.

Meshalkina, N.S., Uralov, A.M., Grechnev, V.V., Altyntsev, A.T., Kashapova, L.K.: 2009, Eruptions of magnetic ropes in two homologous solar events of 2002 June 1 and 2: a key to understanding an enigmatic flare. *Publ. Astron. Soc. Japan* **61**, 791. DOI. ADS.

Metcalf, T.R., Alexander, D.: 1999, Coronal trapping of energetic flare particles: Yohkoh/HXT observations. *Astrophys. J.* **522**, 1108. DOI. ADS.

Nitta, N.V., Aschwanden, M.J., Boerner, P.F., Freeland, S.L., Lemen, J.R., Wuelser, J.-P.: 2013, Soft X-ray fluxes of major flares far behind the limb as estimated using STEREO EUV images. *Solar Phys.* **288**, 241. DOI. ADS.

Ontiveros, V., Vourlidas, A.: 2009, Quantitative measurements of coronal mass ejection-driven shocks from LASCO observations. *Astrophys. J.* **693**, 267. DOI. ADS.

Patsourakos, S., Vourlidas, A., Stenborg, G.: 2013, Direct evidence for a fast coronal mass ejection driven by the prior formation and subsequent destabilization of a magnetic flux rope. *Astrophys. J.* **764**, 125. DOI. ADS.

Pesce-Rollins, M., Omodei, N., Petrosian, V., Liu, W., Rubio da Costa, F., Allafort, A., Fermi-LAT Collaboration: 2015, Fermi Large Area Telescope observations of high-energy gamma-ray emission from behind-the-limb solar flares. In: Borisov, A.S., Denisova, V.G., Guseva, Z.M., Kanevskaya, E.A., Kogan, M.G., Morozov, A.E., Puchkov, V.S., Pyatovsky, S.E., Shoziyoev, G.P., Smirnova, M.D., Vargasov, A.V., Galkin, V.I., Nazarov, S.I., Mukhamedshin, R.A. (eds.) *Proc. 34th Internat. Cosmic Ray Conf. (ICRC2015).* pos.sissa.it/236/128/. ADS.

Plotnikov, I., Rouillard, A.P., Share, G.H.: 2017, The magnetic connectivity of coronal shocks from behind-the-limb flares to the visible solar surface during γ-ray events. *Astron. Astrophys.* **608**, A43. DOI. ADS.

Ramaty, R., Kozlovsky, B., Lingenfelter, R.E.: 1975, Solar gamma rays. *Space Sci. Rev.* **18**, 341. DOI. ADS.

Ramaty, R., Mandzhavidze, N.: 2000, Gamma-rays from solar flares. In: Martens, P.C.H., Tsuruta, S., Weber, M.A. (eds.) *Highly Energetic Physical Processes and Mechanisms for Emission from Astrophysical Plasmas*, *IAU Symp.* **195**, Astron. Soc. Pacific, San Francisco, 123. ADS.

Reames, D.V.: 2013, The two sources of solar energetic particles. *Space Sci. Rev.* **175**, 53. DOI. ADS.

Rouillard, A.P., Plotnikov, I., Pinto, R.F., Tirole, M., Lavarra, M., Zucca, P., Vainio, R., Tylka, A.J., Vourlidas, A., De Rosa, M.L., *et al.*: 2016, Deriving the properties of coronal pressure fronts in 3D: application to the 2012 may 17 ground level enhancement. *Astrophys. J.* **833**, 45. DOI. ADS.

Ryan, J.M.: 2000, Long-duration solar gamma-ray flares. *Space Sci. Rev.* **93**, 581. ADS.

Saito, K., Makita, M., Nishi, K., Hata, S.: 1970, A non-spherical axisymmetric model of the solar K corona of the minimum type. *Ann. Tokyo Astron. Obs.* **12**, 53. ADS.

Scherrer, P.H., Schou, J., Bush, R.I., Kosovichev, A.G., Bogart, R.S., Hoeksema, J.T., Liu, Y., Duvall, T.L., Zhao, J., Title, A.M., *et al.*: 2012, The Helioseismic and Magnetic Imager (HMI) investigation for the Solar Dynamics Observatory (SDO). *Solar Phys.* **275**, 207. DOI. ADS.

Share, G.H., Murphy, R.J., Tolbert, A.K., Dennis, B.R., White, S.M., Schwartz, R.A., Tylka, A.J.: 2017, Characteristics of sustained > 100 MeV gamma-ray emission associated with solar flares. *Astrophys. J.*, Suppl., submitted. arXiv

Silva, A.V.R., Wang, H., Gary, D.E.: 2000, Correlation of microwave and hard X-ray spectral parameters. *Astrophys. J.* **545**, 1116. DOI. ADS.

Uralov, A.M., Grechnev, V.V., Rudenko, G.V., Myshyakov, I.I., Chertok, I.M., Filippov, B.P., Slemzin, V.A.: 2014, A challenging solar eruptive event of 18 November 2003 and the causes of the 20 November geomagnetic superstorm. III. Catastrophe of the eruptive filament at a magnetic null point and formation of an opposite-handedness CME. *Solar Phys.* **289**, 3747. DOI. ADS.

van Driel-Gesztelyi, L., Baker, D., Török, T., Pariat, E., Green, L.M., Williams, D.R., Carlyle, J., Valori, G., Démoulin, P., Kliem, B., Long, D.M., Matthews, S.A., Malherbe, J.-M.: 2014, Coronal magnetic reconnection driven by CME expansion – the 2011 June 7 event. *Astrophys. J.* **788**, 85. DOI. ADS.

Vilmer, N., MacKinnon, A.L., Hurford, G.J.: 2011, Properties of energetic ions in the solar atmosphere from γ-ray and neutron observations. *Space Sci. Rev.* **159**, 167. DOI. ADS.

Vršnak, B., Cliver, E.W.: 2008, Origin of coronal shock waves. Invited review. *Solar Phys.* **253**, 215. DOI. ADS.

Webb, G.M., Axford, W.I., Terasawa, T.: 1983, On the drift mechanism for energetic charged particles at shocks. *Astrophys. J.* **270**, 537. DOI. ADS.

White, S.M., Krucker, S., Shibasaki, K., Yokoyama, T., Shimojo, M., Kundu, M.R.: 2003, Radio and hard X-ray images of high-energy electrons in an X-class solar flare. *Astrophys. J. Lett.* **595**, L111. DOI. ADS.

White, S.M., Benz, A.O., Christe, S., Fárník, F., Kundu, M.R., Mann, G., Ning, Z., Raulin, J.-P., Silva-Válio, A.V.R., Saint-Hilaire, P., Vilmer, N., Warmuth, A.: 2011, The relationship between solar radio and hard X-ray emission. *Space Sci. Rev.* **159**, 225. DOI. ADS.

Wild, J.P., Smerd, S.F., Weiss, A.A.: 1963, Solar bursts. *Annu. Rev. Astron. Astrophys.* **1**, 291. DOI. ADS.

Yashiro, S., Gopalswamy, N., Michalek, G., St. Cyr, O.C., Plunkett, S.P., Rich, N.B., Howard, R.A.: 2004, A catalog of white light coronal mass ejections observed by the SOHO spacecraft. *J. Geophys. Res.* **109**, A07105. DOI. ADS.

Zimovets, I., Vilmer, N., Chian, A.C.-L., Sharykin, I., Struminsky, A.: 2012, Spatially resolved observations of a split-band coronal type II radio burst. *Astron. Astrophys.* **547**, A6. DOI. ADS.